Accelerating and Decelerating Flows in a Rod Bundle

by

Dana Duong

A thesis submitted to the Faculty of Engineering
in partial fulfillment of the requirements for the degree of

MASTER OF APPLIED SCIENCE

in

Mechanical and Aerospace Engineering

Ottawa-Carleton Institute for Mechanical and Aerospace Engineering
University of Ottawa
Ottawa, Canada

August 2017

Abstract

Hot-wire measurements of mean velocity and turbulence parameters were collected at the mid-point of a rod-wall gap and in the centre of a triangular subchannel in accelerating and decelerating flows through a large-scale (12.9:1) model of a 60° section of a CANadian Deuterium Uranium (CANDU) nuclear reactor 37-rod bundle. A method was developed to correct the axial velocity fluctuations for the effects of cycle-to-cycle variations, which were particularly significant during deceleration. Compared to values in stationary flows, the gap vortex street Strouhal number was slightly larger during accelerating flow and smaller during decelerating flow. The integral length scales of the axial velocity at both locations during both acceleration and deceleration were larger than the corresponding values in stationary flow. The Taylor microscale during transients was slightly larger than the stationary values. The turbulent kinetic energy dissipation rate was larger for accelerating flow and smaller for decelerating flow. The opposite was found to be true for the Kolmogorov microscale.

Acknowledgments

I would like to express my sincerest gratitude to my supervisor, Dr. Stavros Tavoularis, for giving me the opportunity to prove to myself that, even with major setbacks during my undergraduate experience, it is possible to succeed. I would not be where I am now without the opportunity he has given me. His guidance as well as kindness have helped me progress further than I thought I could ever achieve. I look forward to continuing my growth under his guidance.

I would also like to thank Stanley Weedmark for his help in teaching me how to machine many of the project parts that were required in this research project, as well as completing parts that could not be finished with the available machines in the student shop. Additionally, I would like to extend my thanks to Leo Denner for aiding me in the electronics work involved with the project.

I would also like to thank my colleagues Armel Don and Dr. Jovan Nedic for their expertise and guidance in my research. From the experiences that I have had with them, I hope to be able to help others as they have done for me.

A special thanks goes to my best friends, Jimmy Truong and Omid Beiraghi, Ehsan Amjadian and younger brother, Donnavon Duong, for being available to keep me company whenever I was in the lab late at night or to just have a chat during my work.

I would like to extend my sincere gratitude to Dr. Ahmedreza Riahi for his help and guidance during my undergraduate experience. Learning from him is an experience I will never forget.

Finally, I would like to thank my parents-in-law, Octavian Barbu and Aurelia Barbu, as well as my own parents, Dong Duong and Yen Le. There is something about being called 'BK Boy' that helped motivate me to pursue an education. My parents-in-law have been especially wonderful, calling and checking up on me, and

ordering me to take breaks. Without their supervision, I most likely would have burned out. I thank them from the bottom of my heart.

I dedicate this experience and thesis to my wife, Roxana-Maria Barbu. Without her, none of this would have been possible. It was her support that encouraged me to apply to a master's degree in the first place. It was her support that kept me going through late nights and stressful times. Her love and companionship were my pillars of strength during any hardship.

Contents

List of Tables

List of Figures

Nomenclature

A, A_0, A_i	hot-wire calibration coefficients
A_c	cross-sectional area of duct
$A_{jet,in}$	jet inlet cross-sectional area
$A_{jet,out}$	jet outlet cross-sectional area
A_P, B_P	pressure transducer coefficients
A_t	cross-sectional area of test section; also cross-sectional area of model
A_T, B_T, C_T	RTD calibration constants
B, B_0, B_i	hot-wire calibration coefficients
b	bias limit
C_ϵ	dissipation parameter
c	relative difference
D	diameter of rod
D_h	hydraulic diameter
E	voltage
E_i	hot-wire voltage
E_t	pressure transducer output voltage
E_θ	voltage at angle θ
f	frequency

f_i, g_i	inclination functions
H	relative humidity
j	$\sqrt{-1}$
k	turbulent kinetic energy
k_{acc}	growth rate constant of sigmoid for accelerating flow
k_{dec}	growth rate constant of sigmoid for decelerating flow
k^2	tangential cooling coefficient
L	integral length scale
N	total number of cycles
n, n_i, n_0	hot-wire calibration coefficient
P	pressure
P_a	ambient room pressure
P_c	wetted perimeter of cross-section
P_d	partial pressure of dry air
P_t	perimeter of model fuel rod
P_v	partial pressure of water vapour
p	precision limit
Q	volumetric flow rate
R	autocorrelation coefficient
R_d	gas constant for dry air

R_o	RTD resistance at 0°C
R_t	radius of pressure tube
R_T	RTD resistance
R_v	gas constant for water vapour
Re	local Reynolds number
$\mathrm{Re}_{\boldsymbol{b}}$	bulk Reynolds number
Re_λ	turbulent Reynolds number
r	radial-axis direction
St	Strouhal number
T	integral time scale
T_a	ambient room temperature
T_{av}	averaging time interval
T_f	jet flow temperature
T_r	reference temperature for α_r
T_R	measured temperature from RTD
T_w	estimated hot-wire sensor temperature
t	time
$t_{50,acc}$	time constant for accelerating flow sigmoid to reach middle value
$t_{50,dec}$	time constant for decelerating flow sigmoid to reach middle value
t_{acc}	time for accelerating flow sigmoid

t_{dec}	time for decelerating flow sigmoid
U	streamwise velocity
U_b	bulk velocity
$U_{high,acc}$	higher velocity asymptote for accelerating flow
$U_{high,dec}$	higher velocity asymptote for decelerating flow
U_i	streamwise velocity for hot-wire sensor, $i = 1, 2$
U_{jet}	jet flow speed
$U_{low,acc}$	lower velocity asymptote for accelerating flow
$U_{low,dec}$	lower velocity asymptote for decelerating flow
U_n	instantaneous velocity for cycle n
U_{sn}	smoothed flow velocity
$U_{sn,acc}$	smoothened accelerating flow velocity for cycle n
$U_{sn,dec}$	smoothened decelerating flow velocity for cycle n
u	instantaneous streamwise velocity fluctuation
u_r	instantaneous radial velocity fluctuation
u_ϕ	instantaneous azimuthal velocity fluctuation
u_{sn}	smoothened velocity fluctuation
V	transverse velocity
V_{ei}	hot-wire effective cooling velocity, $i = 1, 2$
X, Y	tangential cooling coefficient parameters

x	streamwise-axis direction

Greek Symbols

α_r	coefficient of resistivity of hot-wire sensor
α_{OHR}	overheat ratio
β, β_i	inclination angle of hot-wire
γ	yaw angle
γ_0	dimensionless centre frequency
ΔP	pressure difference
Δt	time difference
δx	measurement uncertainty of x
ϵ	turbulent kinetic energy dissipation rate
η	Kolmogorov microscale
θ	angular position
θ_{max}	pitch angle of maximum cross-wire output voltage
λ	Taylor microscale
μ	dynamic visocity of air
ν	kinematic viscosity of air
ρ	air density
σ	standard deviation

τ	time increment
τ_0	time of first zero crossing
ϕ	azimuthal-axis direction
ψ	Morlet wavelet function

Other Notations

$\overline{...}$	time average
$< ... >$	phase average

Subscripts

$(...)_{gap}$	mid-gap
$(...)_{CS}$	centre of central subchannel

Chapter 1

Introduction

1.1 Motivation

Ever since the first nuclear reactor, the Chicago Pile-1, came into operation in 1942, the dependency of humanity on nuclear energy has continued to increase. As of 2012, 11.5% of the global electrical energy production was from nuclear plants. Despite the development of alternative power sources, nuclear power generation is projected to grow in the future. Two of the main challenges that need to be overcome are the extension of the lifetime of current aging nuclear power plants and the development of enhanced safety analysis procedures for current and future power plants.

Among the different types of nuclear reactors, the interest in this thesis is focused on the CANadian Deuterium Uranium reactor (CANDU), which is a Pressurized Heavy Water Reactor (PHWR). Developed in the late 1950s, the CANDU reactor uses non-enriched Uranium as fuel and has the ability to be refueled while in operation. These advantages are the result of the pressure tube design and the use of heavy water as the moderator. The core of the CANDU reactor, called the Calandria, is a cylindrical vessel that contains a number (380 - 480) of pressure tubes, immersed in heavy water that acts as the moderator. Each pressure tube contains a number of fuel assemblies (rod bundles) stacked from end to end. The standard design of a CANDU rod bundle has 37 fuel elements (rods), which contain fuel pellets and are cooled by circulating heavy water. The overall performance, efficiency and safety of the CANDU reactor depends to a great extent on the flow of coolant in the rod bundles.

Nuclear accidents, most prominent of which are the ones in Three Mile Island, Chernobyl and Fukushima, have prompted drastic upgrading in the safety regulations for nuclear reactors. In a number of postulated accident scenarios, coolant flow through the reactor core would be transient. Transient flows would also occur during start-up and shut-down of the reactor. Transient flow and heat transfer could be potentially different from those under corresponding steady conditions and such differences could have an impact on reactor safety analyses. Among the flow properties that could be affected by mean unsteadiness are the structure of the turbulence in different subchannels, the flow distribution among subchannels and the characteristics of the vortex streets that are known to be generated in tightly-packed rod bundles.

1.2 Thesis Objective and Scope

The present work aims to characterize the isothermal turbulent flow of air in a model of a CANDU 37-rod bundle during time intervals in which the mean flow is accelerated or decelerated and to compare these results to values in corresponding steady flows. Measurements include the vortex street frequency, the mean flow, turbulent stresses, the integral length scale, the Taylor microscale, and the Kolmogorov microscale of the turbulence. As representative of the entire rod bundle, measurements were collected at two locations, namely, the mid-point of a rod-wall gap and the centre of a triangular subchannel.

1.3 Organisation of the Thesis

This chapter presents some general background information on nuclear reactors as motivation for this work, as well as the objective, scope and organisation of the thesis. The second chapter provides a review of the relevant literature. The third chapter presents details of the experimental apparatus and methods as well as definitions of properties of interest. The measurements are presented and discussed in the fourth chapter, whereas the fifth chapter outlines the main conclusions and some recommendations for future research.

Chapter 2

Literature Review

The present chapter first presents a review of previous experimental and computational studies on stationary turbulent flows in rod bundles. There is very little literature on non-stationary (casually referred to as transient or unsteady) flows in tightly-packed rod bundles, with the few available studies focusing on heat transfer. For this reason, this chapter outlines available literature on “unsteady” pipe and channel flows, which have some aspects of interest to the present work.

2.1 Steady Flows in Rod-bundles

2.1.1 Experimental Studies

Many experimental studies have been conducted to measure the velocity distribution and the turbulence structure in different rod bundle configurations. One of the earliest studies was conducted by Eifler and Nijsing (1967). They investigated the effects of the Reynolds number and rod spacing on the velocity distribution in a triangular array through the use of a Pitot tube. In their findings, they reported that the Reynolds number had a small effect and the rod spacing had a large effect on the velocity distribution. Unlike flows in pipes and loosely-packed rod bundles, tightly-packed rod bundle flows (namely rod bundles with a pitch-to-diameter ratio that is less than 1.2) contain streets of strong vortices that form on either side of narrow gaps that connect open subchannels (Guellouz and Tavoularis, 2000; Hooper and Rehme, 1984). A historical review of these phenomena was given by Meyer (2010) and a related nomenclature was suggested by Tavoularis (2011). It is generally accepted that these vortices are coherent structures that appear regularly in pairs. Baratto et al. (2006) showed that the vortex streets in different gaps are synchronized and form a vortex network in the entire rod bundle.

In a recent study, Don (2016) examined the dependence of the structure of turbulence in a 60° section of a CANDU 37-rod bundle model on the Reynolds number. He found that the axial velocity distribution was weakly affected by Reynolds number and that the normalised normal Reynolds stresses and the normalised turbulent kinetic energy decreased as the Reynolds number increased. The effect of Reynolds number was weak but measurable on the integral length scales of the axial and radial velocity fluctuations but negligible on the integral length scale of the azimuthal velocity fluctuations, especially in the gap regions. The Taylor and Kolmogorov microscales decreased as the Reynolds number increased. The generation of vortex streets was found to occur close to the inlet of the rod-bundle test section. The convection speed and frequency of these vortex streets increased proportionally to Reynolds number, but the vortex spacing was not affected by the Reynolds number. This study was conducted in the same facility as the present one and will be used as a reference for comparison.

2.1.2 Computational Studies

The results of early computational studies of rod-bundle flows have been known to differ greatly from experimental results (Meyer, 2010). However, in recent years, numerical simulations of turbulent flow and heat transfer in rod bundles have provided fair to good predictions of flows through rod bundles, including tightly-packed ones.

Chang and Tavoularis (2005) solved the Unsteady Reynolds Averaged Navier-Stokes (URANS) equations to simulate numerically the formation of coherent vortices and their effects on the flow structure in a rectangular channel with a circular rod (rectangular annulus) and reported that most of the turbulent kinetic energy in the gap region was associated to these vortices. Chang and Tavoularis (2007) further used URANS, coupled with a Reynolds stress model, to compute the turbulence characteristics in the flow of a 60° section of a CANDU 37-rod bundle. Their results were in good agreement with experimental work. Chang and Tavoularis (2012) performed a comparative study between Reynolds Averaged Navier-Stokes (RANS) solutions, URANS solutions and Large-Eddy Simulations (LES) for a rectangular annulus and concluded that LES yielded the most accurate results, although URANS results were fairly accurate as well.

2.2 Unsteady Flows

There is no literature that addresses directly vortex streets in unsteady flows in tightly-packed rod bundles. The few available experimental and numerical studies on unsteady heat transfer are only indirectly relevant to the present interests. Somewhat relevant is also the literature on periodic pulsating flows and non-periodic transient flows in pipes and channels, although these contain no vortex streets.

2.2.1 Experimental Studies

Hong et al. (2003) and Hong et al. (2004) performed two experiments: a pressure-decreasing transient critical heat flux (CHF) experiment in a vertical annulus using refrigerant R-134a and a steady CHF experiment in the same test section and with the same working fluid, which was used as a reference for comparisons. In two other studies, Chun et al. (2009) and Watanabe et al. (2011) examined heat transfer during increasing and decreasing pressure transients through the critical pressure in a 5 × 5 rod bundle cooled by R-134a and compared the results. Kang and Chang (2009) studied the effects of pressure transients on the heat transfer in a vertical tube cooled by R-134a and found that the rate of pressure change had an impact on the heat transfer coefficient in the subcritical pressure region. None of the previously mentioned studies provided any information concerning the flow structure.

Pulsating turbulent pipe flows have been studied extensively due to their frequent occurrence in numerous applications. Some early studies used electrolysis (Gerrard, 1971), single-component Laser Doppler Anemometry (Ramaprian and Tu, 1980,1983; Tu and Ramaprian, 1983), and hot-wire anemometry (Shemer and Kit, 1984; Shemer et al., 1985). Some authors (Ramaprian and Tu, 1980,1983; Tu and Ramaprian, 1983) investigated the dependence of the turbulence fields on the frequency of the imposed oscillations. An interesting observation was that the Reynolds stresses remained frozen during the cycle at high frequencies, while other turbulence properties deviated from the steady state. Shemer and Kit (1984) concluded that, when the frequency of the pulsations was sufficiently high, the turbulence did respond to the changes in the mean flow, so that the turbulence structure became independent of the pulsations. Shemer et al. (1985) further observed that the amplitude of oscillations affected the turbulence fields to a lesser extent in comparison to the oscillation frequency. A review of early works of these types of flows was done by Brereton and Mankbadi (1995). In a more recent study, He and Jackson (2009) examined a pulsating turbulent pipe flow using a two-component LDA system and found that the response of turbulence to flow oscillations initially occurred in the wall region and then propagated across the core. They also found that the time delay of the response of turbulence in the core was independent of the frequency of oscillation but decreased with increasing mean flow rate.

Due to the difficulty in generating non-pulsating transient flows, very few studies of such flows have been conducted. One of the earliest studies by Maruyama et al. (1976) examined the turbulence response following a step increase or decrease in the flow rate of a turbulent pipe flow. The authors found that, in the step increase case, generation and propagation of new turbulence occurred, whereas, during the step decrease case, there was a decay of the existing turbulence. In a more recent study, He and Jackson (2000) used a two-component LDA system to make simultaneous measurements of either the axial and radial or the axial and azimuthal components of the velocity in a ramp-type transient flow. In their flow loop facility, flow control of the ramp-type flow was achieved by adjusting a pneumatically operated, computer-controlled valve situated downstream of their test section. Phase-averaged velocities, root-mean-square velocity fluctuations and turbulent shear stresses were determined from the measurements. These authors identified three types of delay: a delay in the response of the turbulence production, a delay in turbulence energy redistribution among the three components, and a delay in the radial propagation of turbulence. In another study, Greenblatt and Moss (2004) investigated the effects of a rapid temporal acceleration in a turbulent pipe flow. These authors concluded that the generation of turbulence occurred in a region away from the wall, contradicting the findings of Maruyama et al. (1976) and He and Jackson (2000). In an extensive study, Tardu and Da Costa (2005) examined several turbulence parameters in a turbulent channel flow subjected to velocity oscillations.

2.2.2 Computational Studies

Early computational studies of transients in pipe flows and channel flows using simple turbulence models had poor agreement with experimental results. Examples of such studies are those by Ohmi and Usui (1976), Ohmi et al. (1978), Murphy and Prenter (1981), Cook et al. (1985), Kirmse (1979), Cousteix et al. (1981) and Blondeaux and

Colombini (1985).

As computational power and turbulence models improved, more accurate CFD studies began to emerge. Examples of such studies are the ones by He et al. (2016), Seddighi et al. (2015), He et al. (2015), He and Seddighi (2015), and Seddighi et al. (2014). These studies include direct numerical simulations (DNS) of a pipe flow with a step increase in flow rate (He et al., 2016), a three-stage transition in transient turbulent channel flow (He et al., 2015), and DNS of an accelerating channel flow (Seddighi et al., 2014). The results of these simulations are in better agreement with experimental data in comparison to the earlier studies.

Chapter 3

Experimental Facility, Instrumentation and Measurement Procedures

This chapter gives an overview of the experimental facility, the instrumentation, the experimental techniques and correction procedures and the measurement uncertainty. Information on the facility and its components has been in part taken from Rind and Tavoularis (2012). Calibration techniques and methods have been taken in part from Don (2016) and Bailey (2006).

3.1 Rod-bundle Test Facility

This section describes the experimental facility, which is shown in Figure 3.1. Its main parts are an intake contraction, a centrifugal blower, a diffuser, a bypass branch, a plenum, and the test section.

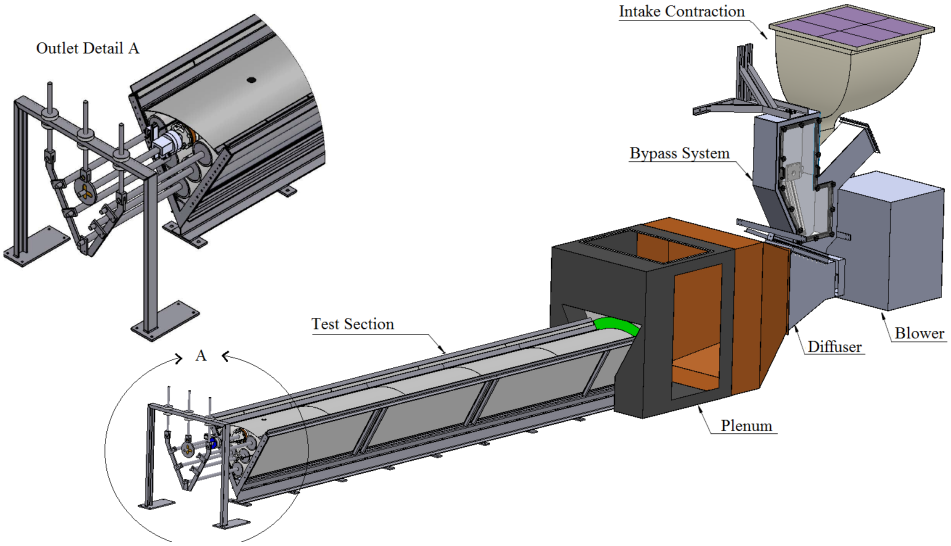

Figure 3.1: Rod-bundle test facility at the University of Ottawa.

3.1.1 Intake Contraction and Blower

The intake contraction was constructed from 3 mm (1/8 in) thick welded 6061 Aluminium sheets. Its design was described by Rind and Tavoularis (2012). It has a 1110 mm × 1111 mm inlet cross-section and a 251 mm × 302 mm throat cross-section, so that the contraction ratio is approximately 16.27. Its length is 1770 mm. The intake of the contraction is covered with a fibreglass filter, which was designed to remove 85% of particles with a diameter 1 μm. Air is accelerated through the intake contraction into a centrifugal blower (Canadian Blower and Forge Co. Ltd., Model 71G-2526T), which discharges it in the diffuser.

3.1.2 Diffuser and Plenum

The diffuser and the plenum, shown in Figure 3.2, were also was made from welded 3 mm thick aluminium sheets. The diffuser consists of an upstream section and a downstream one. The upstream section contains a bypass port leading into the bypass section. The upstream section has an inlet cross-section that is 406 mm high and 343 mm wide and an outlet cross-section that is 910 mm high and 343 mm wide. The length of the upstream section is 762 mm. The downstream section contains five perforated plates (type A, Table 3.1), which are meant to break down large-scale air motions as well as preventing flow separation from the diffuser walls. The downstream section has an inlet cross-section that is 910 mm high and 343 mm wide and an outlet cross-section that is 1645 mm high and 1391 mm wide. The length of the downstream section is 1016 mm. To reduce the vibrations generated from the blower, a rubber coupling was used to connect the diffuser to the blower.

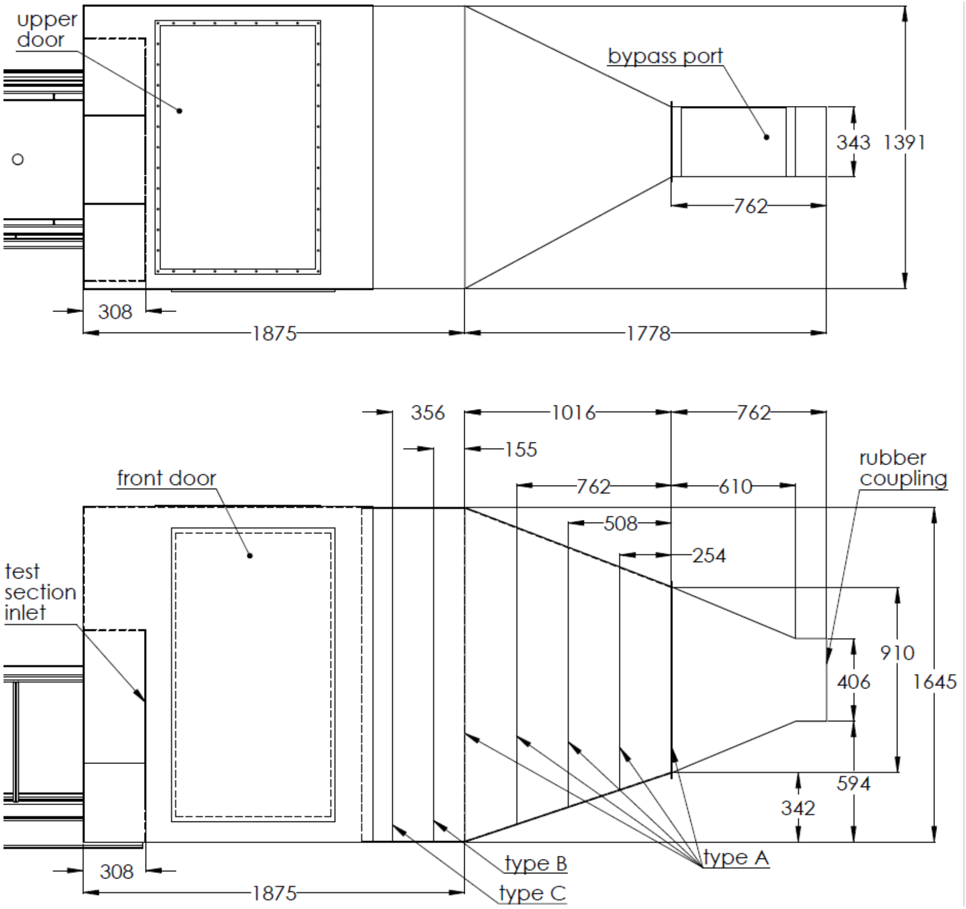

Figure 3.2: Front and top view schematic diagrams of the diffuser and the plenum (Rind and Tavoularis, 2012). Dimensions are in mm.

The plenum is a chamber 1875 mm long, 1645 mm high and 1391 mm wide. It has an upper and a front access door. To straighten and improve the uniformity of the flow and further reduce the turbulence at the test section inlet, a honeycomb (type

B, Table 3.1) and a perforated plate (type C, Table 3.1) were installed across the plenum (Figure 3.2).

Table 3.1: Perforated plate specifications (Don, 2016).

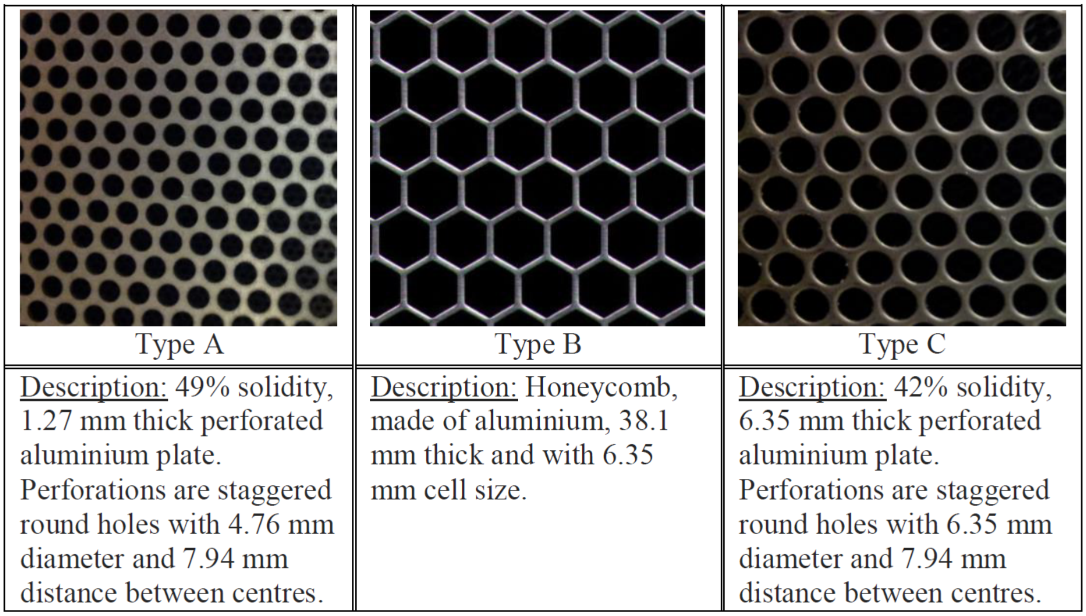

Type A	Type B	Type C
Description: 49% solidity, 1.27 mm thick perforated aluminium plate. Perforations are staggered round holes with 4.76 mm diameter and 7.94 mm distance between centres.	Description: Honeycomb, made of aluminium, 38.1 mm thick and with 6.35 mm cell size.	Description: 42% solidity, 6.35 mm thick perforated aluminium plate. Perforations are staggered round holes with 6.35 mm diameter and 7.94 mm distance between centres.

3.1.3 Bypass Section

A bypass section (Figure 3.3) is connected to the bypass port of the diffuser (Figure 3.4). The bypass section contains a custom-made, hinged flap, which is operated by a linear actuator (Parker Hannifin Corporation, Model ETH080M32A1XPWDSN600A). There are two extreme positions of the flap: one for which the bypass branch is fully closed and all flow passes through the test section, and another for which the main branch leading to the test section is closed and all flow passes through the bypass branch. At the maximum velocity of the actuator, the flap can move from one extreme position to the other in approximately 1.5s. The range and speed of the actuator is adjusted using a controller (Parker Hannifin Corporation, Model S150V2F11I11T30M00) connected to a computer. This allows the programming of various types of transient mass flow rates through the test section.

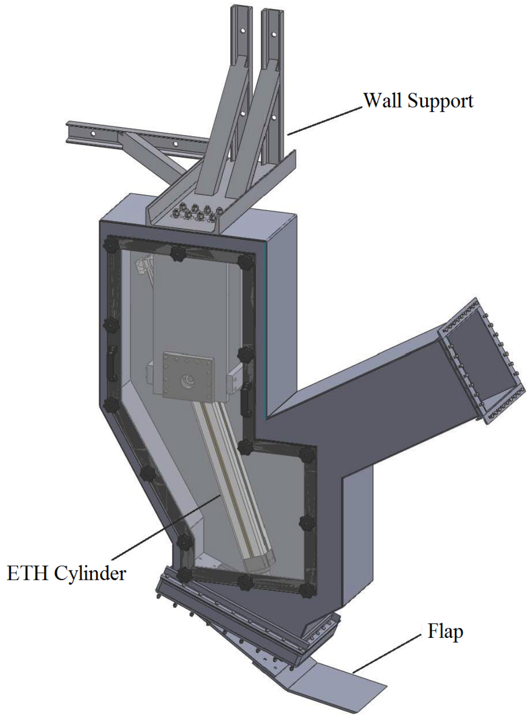

Figure 3.3: Bypass section.

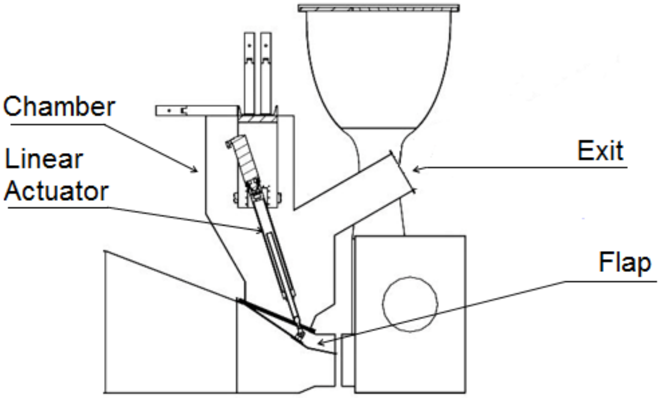

Figure 3.4: Schematic diagram of the bypass section connected to the test facility (Rind and Tavoularis, 2012).

3.1.4 Test Section

The test section is a scaled up, 12.9:1, model of a 60°section of the CANDU 37-rod bundle. It consists of six rods and a one-sixth section of a rod, modeled after

CANDU fuel elements. A cross-section view of the test section at the inlet is presented in Figure 3.5. With the exception of the central rod, all others are made of a Schedule 40 aluminium pipe with a diameter of 168.3 mm and a length of 6100 mm, which give a length-to-diameter ratio of approximately 36.2. The diameter and length of a standard CANDU rod are 13.08 mm and 500 mm, resulting in a length-to-diameter ratio of 38.2, slightly larger than the value in the present facility. The central rod, shown in Figure 3.5, is made of a Schedule 40 polyvinyl chloride (PVC) pipe, mounted co-axially on an internal Schedule 10 aluminium rod of 101.6 mm diameter, so that it can be traversed on a cross plane. The PVC shell was built in preparation for future studies, for which it can be covered with a thin metallic foil that can be heated electrically for heat transfer studies. The internal aluminium rod was used to reduce sagging and was kept in place by several spacers. The maximum sag of the top central rod was 0.8 mm, and the maximum sag of the other rods was estimated at about 0.2 mm. In most cases, the change of the gap size at the location of maximum sag of each rod was less than 3%. The uncertainty of the rod diameter is 0.42 mm.

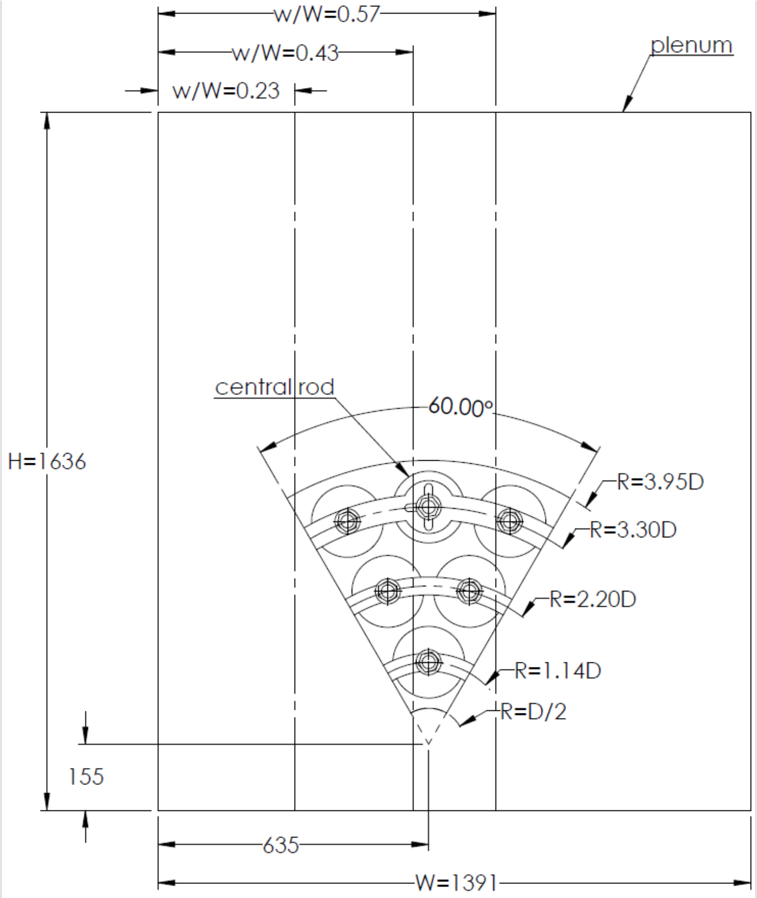

Figure 3.5: Cross-section view of test section inlet with endplate (Rind and Tavoularis, 2012). Dimensions are in mm.

A model of the CANDU endplate, made of aluminium, supports the rods at the upstream end. The endplate is 13.6 mm thick. At the downstream end, the test section rods are supported by 38.1 mm diameter aluminium coaxial rods fastened to a 13.6 mm thick aluminium frame, located 700 mm away from the test section outlet. This is shown in Figure 3.5.

The cover of the test section is composed of 1 mm thick, curved stainless steel sheets, separated into five sections. The sheets emulate the CANDU pressure tube. Each sheet contains a port, allowing vertical insertion and traversing of probes along the gap subchannel between the top central rod and the inner wall of the top cover. The distances of the port centres from the inlet are listed in Table 3.2.

Table 3.2: Positions of port centres on the cover of the test section from the inlet.

Port number	1	2	3	4	5
Distance from the inlet (mm)	406	2032	3251	4470	5690

The minimum rod-wall gap width is 25.25 mm ($\approx 0.15D$), whereas the minimum rod-rod gap width is 23.56 mm ($\approx 0.14D$). Spacers were inserted in the narrow gaps at the downstream end of the test section with the exception of the gaps around the central rod to maintain nominal gap distances. Spacers were also inserted half-way along the test section in the gaps between the rods and the side walls. The side walls of the test section was made of 10 mm thick glass with matching acrylic sections located at four locations along the test section. The walls were adjusted and fastened with horizontal clamps to prevent significant deformation and leakage.

Traversing System

A hot-wire traversing system was mounted on the support of the central rod at the exit of the test section. This is shown in Figure 3.6. It consists of a single-axis linear slide (Velmex Inc, model MA1505-25K1) and a rotary table (Velmex Inc, model B4836TS-ZRS), controlled by two programmable stepper motor encoders (Velmex Inc, model VXM-1). The linear slide allowed radial positioning of the hot-wire probe. When operated in half-step mode, the linear slide has a resolution of 0.0025 mm/step with a 0.18 mm positioning uncertainty. The rotary table allowed angular positioning of the hot-wire probe, with a resolution of 0.025°/step and a positioning uncertainty of 0.11°. A pitch alignment mount on the linear slide was used to align the axis of the probe parallel to the incoming flow.

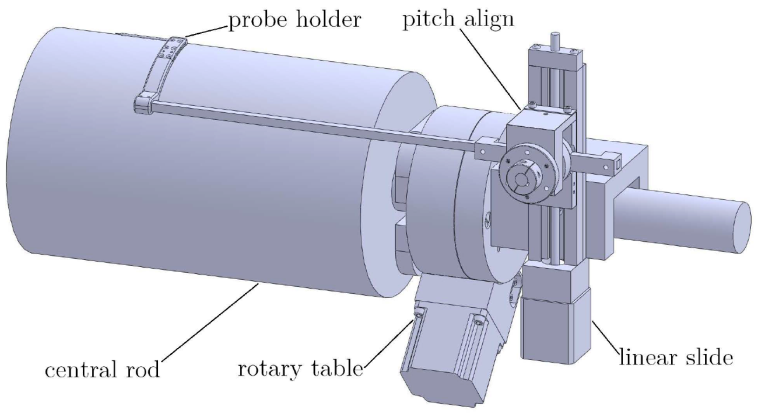

Figure 3.6: Hot-wire traversing system at the end of the test section (Don, 2016).

3.2 Calibration Facility

Hot-wire velocity and directional calibrations for the test section were undertaken on the calibration jet facility presented in Figure 3.7. It consists of a nozzle unit (Dantec Dynamics, model 55DH5) and two rotary tables (Velmex Inc, model B5990TS) controlled by two controllers (Velmex Inc, model VXM-1). Further details on the calibration facility are provided by Bailey (2006).

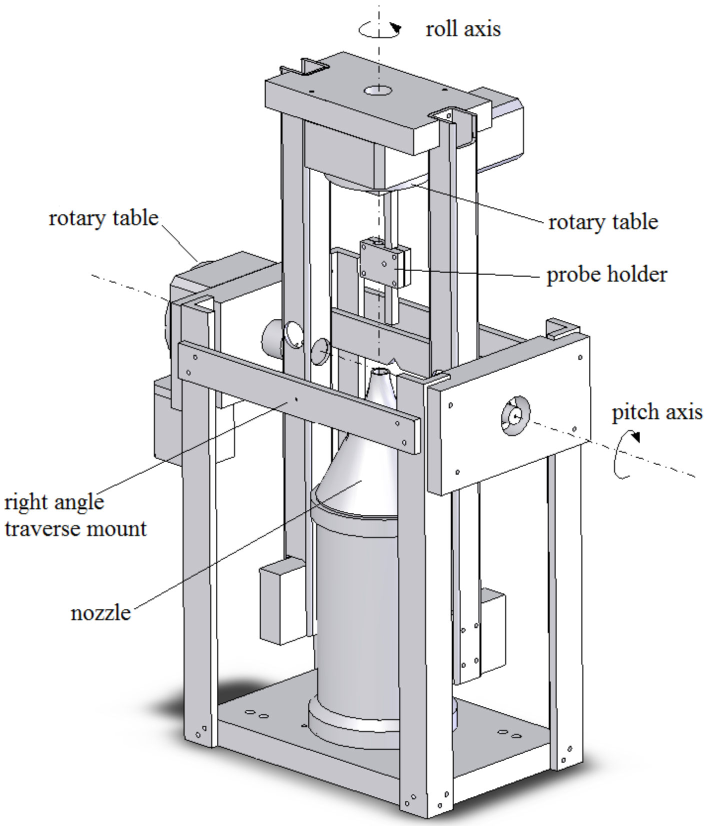

Figure 3.7: Calibration jet (Bailey, 2006).

For calibrating right-angle hot-wire probes, two additional degrees of freedom were added to the original calibration facility. The set up, shown in Figure 3.8, consists of a single-axis linear slide, a high resolution stepper motor (Oriental Motor, model PKP244MU12A-L) and a 50:1 ratio worm-drive gearbox. The right-angle probe was mounted onto the worm wheel enabling rotation about its axis for directional and yaw calibrations. The angular positioning resolution of the combined worm-drive/stepper motor was 0.01°/step with a positioning uncertainty of 0.09°. The linear slide was programmed to correct for the displacement caused by the rotation of the probe during calibration. The right-angle hot-wire calibration system was mounted onto the calibration jet at the location shown in Figure 3.7.

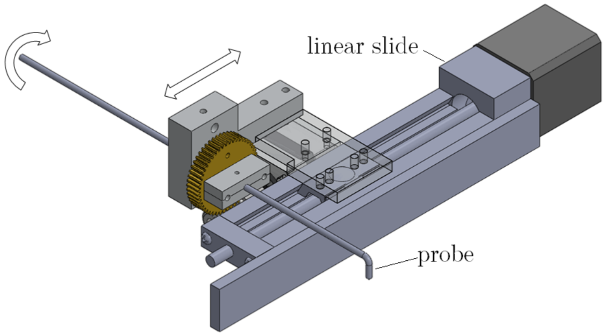

Figure 3.8: Right-angle cross-wire probe calibration traversing system (Don, 2016).

3.3 Instrumentation

This section describes the instrumentation used in this investigation.

3.3.1 Hot-wire Anemometry

The measurement technique used in this experiment was constant temperature hot-wire anemometry (HWA). HWA measures flow velocity from the convective heat transfer from a heated wire or film placed in a fluid flow and is mostly used for gas/air flow studies. Advantages of HWA include an excellent frequency response and a high signal-to-noise ratio (Bruun, 1995). Four hot-wire probes were used in this study: a straight cross-wire probe, a right-angle cross-wire probe, and two single-wire probes.

Straight Cross-wire Probe

A straight cross-wire probe (Auspex Scientific, Model AHWX-100), made of Platinum-coated Tungsten wires arranged in an X-array, shown in Figure 3.9, was mounted at the exit of the test section for mean velocity and turbulence measurements. The sensor dimensions are 1 mm in length and 5 μm in diameter. The separation distance between the sensors is approximately 0.5 mm. The inclination angle $\overline{\alpha}$ of each sensor with respect to the probe axis is nominally 45°, but its exact value was determined through a yaw angle probe calibration.

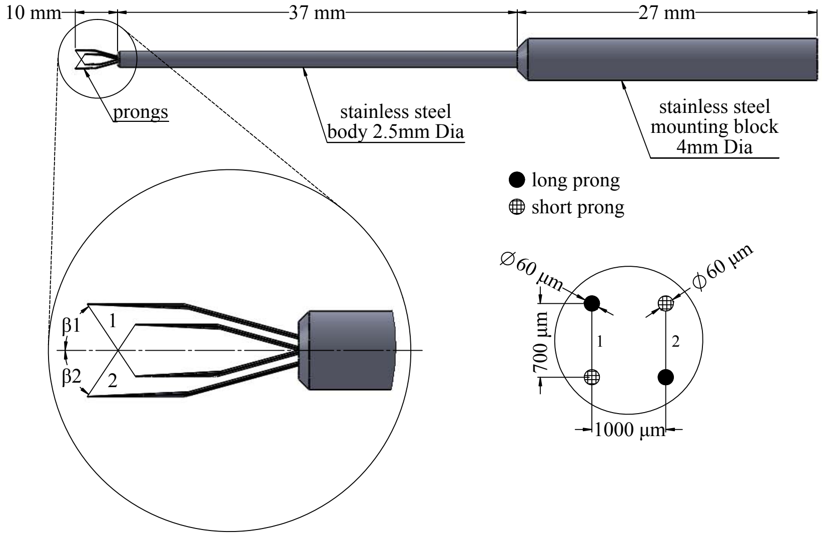

Figure 3.9: Sketch of the straight cross-wire probe. Dimensions are in mm.

Right-angled Cross-wire Probe

A right-angled cross-wire probe, custom built by Auspex Scientific and shown in Figure 3.10, was mounted on the top cover ports to measure the gap subchannel velocity and turbulence parameters. The probe has two 5 μm diameter, 1 mm long Platinum-coated Tungsten wires arranged in an X-array. The distance between the sensors is approximately 0.5 mm.

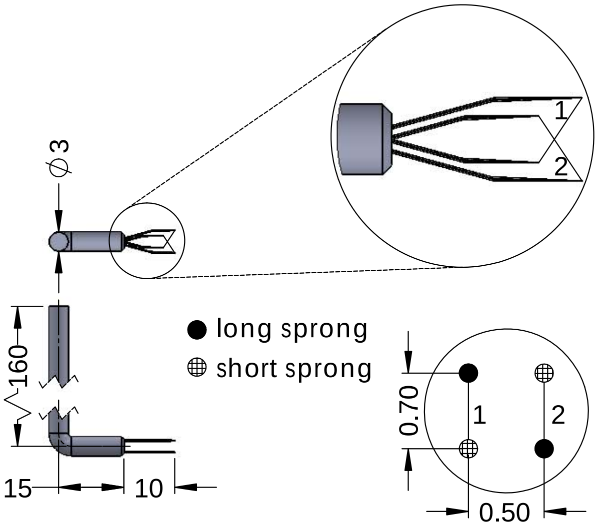

Figure 3.10: Sketch of the right-angle cross-wire probe (Don, 2016). Dimensions are in mm.

Single-wire Probe

Two single-wire (Dantec Dynamics, Model 55P11) probes were used for velocity measurements at the bypass exit and in the intake contraction. The probes have a single 5 μm diameter, 1.25 mm long Platinum-coated Tungsten wire.

Anemometer

Three A.A. Labs anemometers were used in this experiment, two Models AN-1002 and one Model AN-1003. The AN-1002 anemometers had two identical removable channels that could be operated at 1:1 and 1:10 bridge ratios. The AN-1003 anemometer has ten identical removable channels. The usable sensor resistance range is $0.5 - 99.9\ \Omega$ and $1 - 9.99\ \Omega$ for the 1:1 and 1:10 bridge ratios, respectively. Each channel has a signal conditioning unit capable of amplifying, offsetting and filtering the hot-wire signal. The low-pass filter in the signal conditioner is a cascade double-pole, low-pass filter with twelve selectable cut-off frequencies. For the AN-1002 channels the cut-off frequency range is from 1.5 kHz to 21 kHz, whereas for the AN-1003 channels it is from 380 Hz to 14.0 kHz. The frequency response of each anemometers depends on the hot-wire probe and the settings used. Hot-wire probes were connected to the anemometer with 5 m, 21-gauge, Alpha Wire-J coaxial RG-58 cables.

3.3.2 Pressure Transducer

A pressure transducer (Furness Control, model FC0332) was used for hot-wire velocity calibrations in this study. It has a pressure range from 0 to 2.5 KPa and an uncertainty of 0.25% of full range.

3.3.3 Resistance Thermometers

A resistance temperature detector (RTD; Rdf Corporation, Model 29348-T01) was mounted beside the straight cross-wire probe to measure the mean flow temperature. The RTD probe was 1.67 mm in diameter and 15.25 mm in length. The relationship between the resistance R_T of the RTD in Ω and the temperature T_R in °C is given by

$$R_T = R_o \left[1 + A_T T_R + B_T T_R^2 + C_T (T_R - 100) T_R^3\right] \tag{3.1}$$

where R_o is the resistance at 0°C, A_T, B_T and C_T are the calibration coefficients. The calibration coefficients were specified by the manufacturer as $R_o = 99.98\ \Omega$, $A_T = 3.916 \times 10^{-3}$, $B_T = -5.998 \times 10^{-7}$ and $C_T = -2.454 \times 10^{-2}$. The RTD measurement was used for correcting the hot-wire velocity measurements for the difference between the jet temperature during calibration and the fluid temperature in the test section during measurement (Bruun, 1995). The measurement uncertainty of the RTD was 0.1 °C.

3.3.4 Weather Forecast Board and Estimation of Air Density

A USB weather board (Sparkfun Electronics, Model V3) and a mercury barometer were used to estimate the air density. The air density was calculated as

$$\rho = \frac{P_d}{R_d T_a} + \frac{P_v}{R_v T_a} \tag{3.2}$$

where P_d is the partial pressure of dry air, P_v is the partial pressure of water vapour, T_a is the ambient room temperature in K, $R_d = 286.9$ J kg^{-1} K^{-1} and $R_v = 461.5$ J kg^{-1} K^{-1}. P_v and P_d were calculated as

$$P_v = 610.78H \times 10^{(7.5T_a/(T_a+237.3))} \tag{3.3}$$

and

$$P_d = P_a - P_v \tag{3.4}$$

where H is the relative humidity of the room and P_a is the ambient room pressure, measured by the barometer.

3.4 Calibration and Signal Processing Methods

3.4.1 Pressure Transducer Calibration

The relationship between the pressure difference and the output voltage is given as

$$\Delta P = A_P E_t + B_P, \tag{3.5}$$

where E_t is the transducer output voltage and A_P and B_P are calibration coefficients. The calibration was performed on the calibration jet over the range of Reynolds number of interest. The calibration data was fitted to a line to determine A_P and B_P. A typical calibration curve is shown in Figure 3.11.

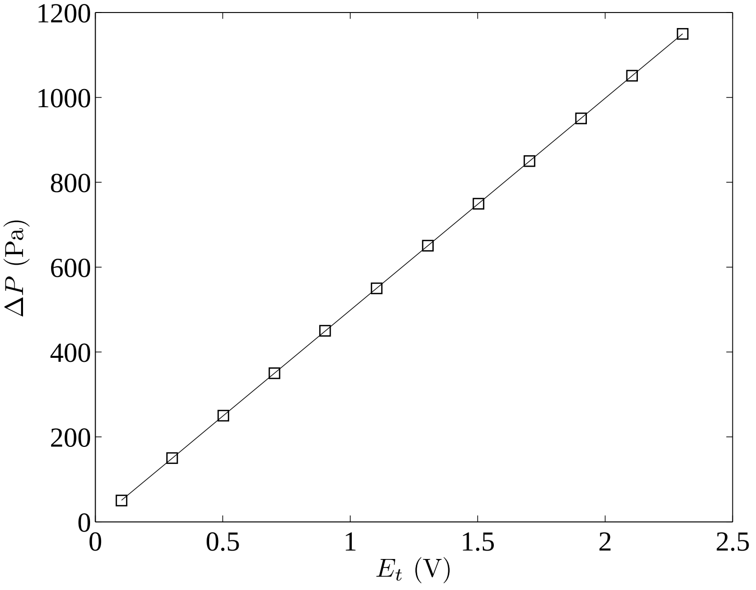

Figure 3.11: Pressure transducer calibration results. Solid line represents fitted line.

3.4.2 Hot-wire Calibration and Signal Processing

Cross-wire Directional Calibration

The directional calibrations were carried out on the calibration jet described by Bruun (1995) and Don (2016). Determining the inclination angle β and tangential cooling coefficient k^2 were the main purposes of the directional calibration. The coefficients resulting from this calibration were used in the final velocity calibration. The following are the calibration steps:

- Step 1: Determination of Sensor Inclination

The cross-wire probe was placed at the centre of the jet. The probe was then rotated about its axis until the sensors were parallel to the plane containing the roll axis and normal to the pitch axis. This was completed using a combination of a digital inclinometer and visual indicators. Using the rotary table along the pitch axis, the probe was tilted in one direction from 35° to 55° at 1° increments to determine the inclination angle β with respect to the probe axis. The data were fitted to a fifth-order polynomial. β was found at the fitted pitch angle θ_{max} at which the voltage reading from the anemometer was maximum. The inclination angle was then calculated as

$$\beta = 90 - \theta_{max}. \tag{3.6}$$

This was repeated in the opposite direction to determine θ_{max} of the other sensor. A typical plot of the anemometer output voltage (E) versus pitch angle at constant velocity is shown in Figure 3.12.

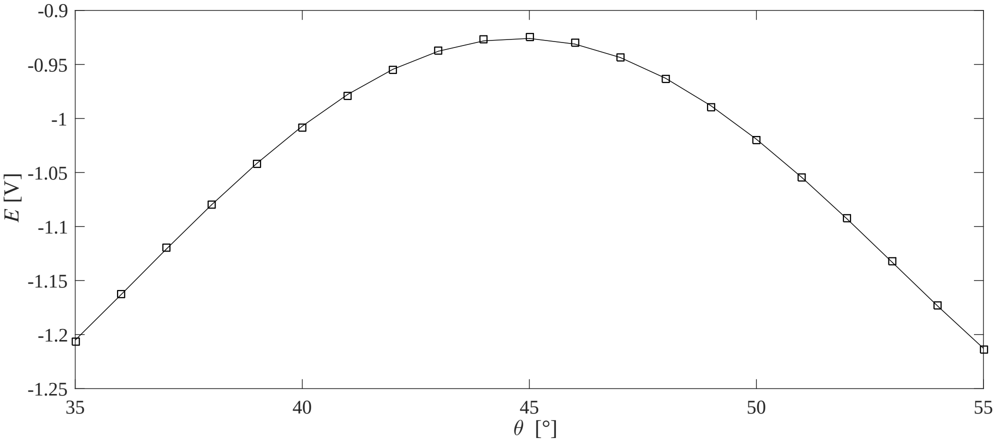

Figure 3.12: Hot-wire voltage output at different inclinations. Solid line indicates a fitted fifth-order polynomial.

- Step 2: Preliminary Velocity Calibration

The relationship between the voltage E of each sensor and the jet flow velocity U_{jet} is described by the modified King's Law

$$\frac{E^2}{T_w - T_f} = A_0 + B_0 U_{jet}^{n_0}, \tag{3.7}$$

where A_0, B_0, and n_0 are calibration coefficients, T_w is the estimated sensor temperature and T_f is the jet flow temperature. T_w was estimated as

$$T_w = (\alpha_{OHR} - 1)/\alpha_r + T_r, \tag{3.8}$$

where $\alpha_r = 0.0048$ °C^{-1} is the sensor's coefficient of resistivity at a reference temperature $T_r = 21° \ C$ (given by the manufacturer) and α_{OHR} is the overheat ratio, set at 1.5 in this study. Values of E and T_f were recorded for at set U_{jet} and least-squares curve fitting was performed to determine the coefficients A_0, B_0, and n_0.

- Step 3: Determination of Tangential Cooling Coefficient

The probe was inclined at various pitch angles ranging from -15° to 15° at 2° increments. At each angular position θ, values for E, U_{jet} and T_f were recorded. Parameters X and Y at each position were calculated as

$$X = E_\theta^2 sin^2\beta - sin^2\gamma Y = E_\theta^2 - 1 \tag{3.9}$$

where the yaw angle γ was determined as

$$\gamma = \theta + \beta. \tag{3.10}$$

and linear curve fitting was performed to find k^2 from the expression

$$Y = (1 - k^2)X. \tag{3.11}$$

The parameter E_θ was estimated as

$$E_\theta = \frac{\left(\frac{E^2/\left(T_w - T_f\right) - A_0}{B_0}\right)^{1/n_0}}{U_{jet}} \tag{3.12}$$

A typical calibration curve is shown in Figure 3.13. The tangential cooling coefficient k^2 of the straight cross-wire probe was approximately 0.025 for both sensors. The tangential cooling coefficient k^2 of the right-angle cross-wire probe was approximately 0.009 for both sensors.

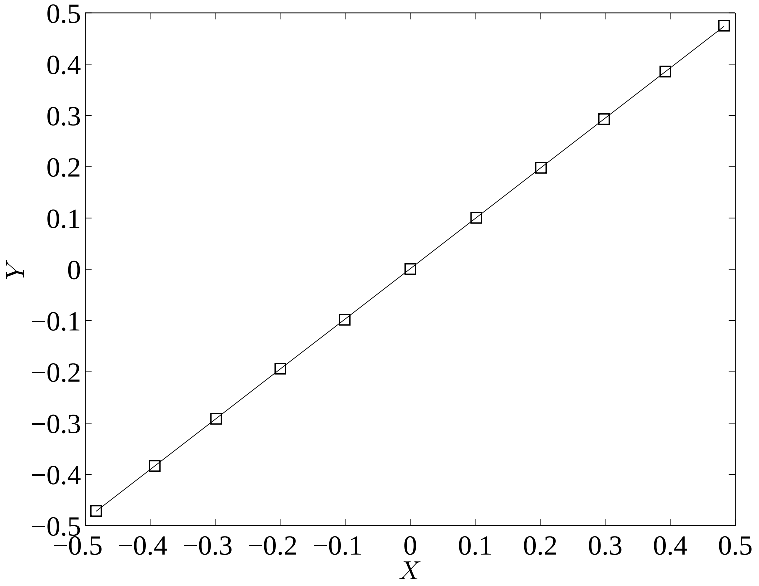

Figure 3.13: Example of yaw calibration result. Solid line indicates linear curve fit.

Cross-wire Velocity Calibration

A similar procedure as the one described in Step 2 was used to determine the calibration coefficients A, B and n for each sensor in the modified King's Law accounting for cooling due to tangential velocity, as described by Bruun (1995), shown below as

$$\frac{E^2}{T_w - T_f} = A + B\left(\left(cos^2\beta + k^2 sin^2\beta\right)^{1/2} U_{jet}\right)^n \tag{3.13}$$

An example of cross-wire calibration curves is shown in Figure 3.14.

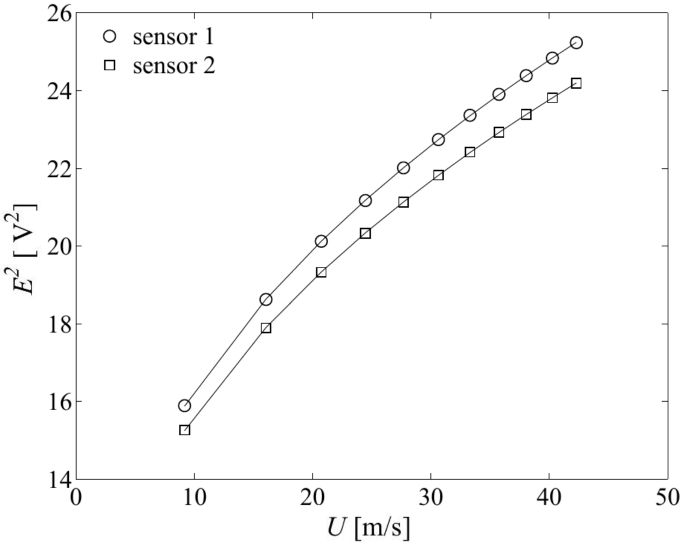

Figure 3.14: Cross-wire velocity calibration results. Solid lines indicate King's Law curve fits.

Single-wire Velocity Calibration

A similar procedure as the one described in the cross-wire method was used for the single-wire probes. However, the directional calibration was not required, and the data were fitted directly to the modified King's law. An example of the single-wire calibration curve is shown in Figure 3.15.

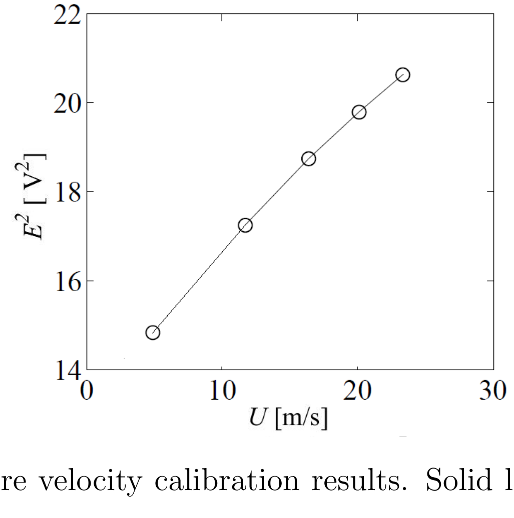

Figure 3.15: Single-wire velocity calibration results. Solid lines indicate King's Law curve fit.

Signal Analysis Method

The cross-wire signal conditioning was carried out in terms of the effective cooling velocities V_{e1} and V_{e2} for the two sensors. The general expression of the effective cooling velocity is

$$V_{ei} = \left(\frac{E_i^2/\left(T_w - T_f\right) - A_i}{B_i}\right)^{1/n_i} \quad , \tag{3.14}$$

where $i = 1$ and $i = 2$ correspond to sensor 1 and sensor 2, respectively. The streamwise and transverse velocities were expressed as

$$U = \frac{\left[V_{e1}/f_1\left(\beta_1\right)\right] g_2\left(\beta_2\right) + \left[V_{e2}/f_2\left(\beta_2\right)\right] g_1\left(\beta_1\right)}{g_1\left(\beta_1\right) + g_2\left(\beta_2\right)} \tag{3.15}$$

$$V = \frac{\left[V_{e2}/f_2\left(\beta_2\right)\right] - \left[V_{e1}/f_1\left(\beta_1\right)\right]}{g_1\left(\beta_1\right) + g_2\left(\beta_2\right)}. \tag{3.16}$$

From the sensor inclination angle β_i, the functions $f_i\left(\beta_i\right)$ and $g_i\left(\beta_i\right)$ were defined as

$$f_i\left(\beta_i\right) = \left(cos^2\beta_i + k_i^2 sin^2\beta_i\right)^{1/2} \tag{3.17}$$

and

$$g_i\left(\beta_i\right) = \frac{\left(1 - k_i^2\right) cos^2\beta_i}{cos^2\beta_i + k_i^2 sin^2\beta_i} \times tan\beta_i. \tag{3.18}$$

After each calibration, velocity tests were conducted on the calibration jet at random velocities within the range of calibration. An example of velocity tests is shown in Figure 3.16.

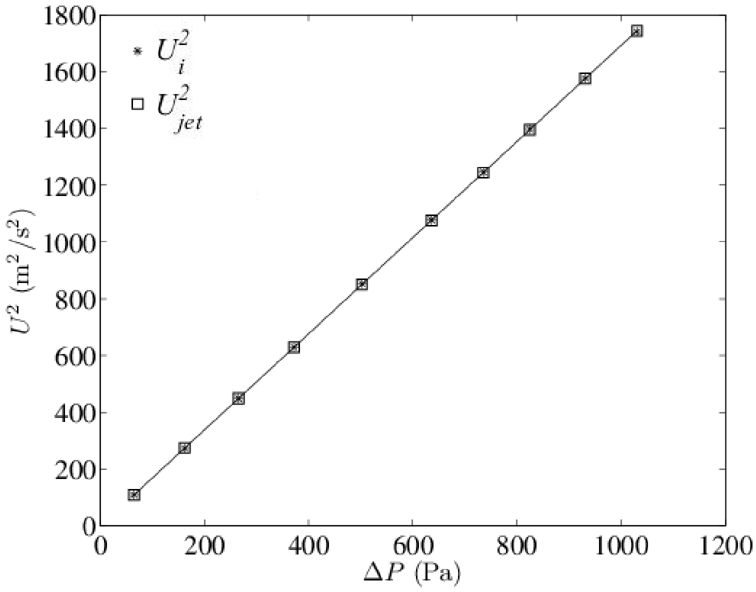

Figure 3.16: Example of velocity tests after calibration. Solid line indicates linear curve fit.

Calibrations were repeated if the relative difference, c, between the hot-wire streamwise velocity U_i and the velocity of the calibration jet U_{jet} exceeded 0.5%. c was calculated as

$$c = 100 \times \sqrt{\frac{1}{N}\sum_{i=1}^{N}\left(\frac{U_i - U_{jet}}{U_{jet}}\right)^2}. \tag{3.19}$$

U_{jet} was calculated as

$$U_{jet}^2 = \frac{2}{\rho\left[1 - (A_{jet,out}/A_{jet,in})^2\right]}\Delta P \tag{3.20}$$

where $A_{jet,out}$ and $A_{jet,in}$ are the jet outlet and inlet cross areas, respectively.

3.4.3 Data Acquisition Systems (DAQ)

Three data acquisition systems were used in this study: a National Instrument (NI) PCI-6143 data acquisition card, a NI cDAQ-9217 data acquisition module, and a NI cDAQ-9263 module. Both the NI cDAQ-9217 and the NI cDAQ-9263 modules were installed on a NI cDAQ 9174 4-slot chassis.

The NI PCI-6143 module has eight dedicated ADC 16-bit analog input channels. It is capable of simultaneous sampling at 250 kHz per channel. It has an analog input signal range of ±5 V. A shielded BNC adapter block (National Instruments, Model BNC-2110) was used to transfer the analog input signals to the data acquisition card. This module was used to take all hot-wire (cross-wire and single-wire) and Pitot-static tube measurements.

The NI cDAQ-9217 module has four 24-bit analog input channels and a sampling rate of 100 Hz per channel. This module was used to digitize the RTD analog input. The RTD readings were converted to temperature using the calibration information provided by the manufacturer.

The NI cDAQ-9263 module has four channels that update their analog outputs at a rate of 100 kHz per channel simultaneously. Each channel has an AO terminal and a common terminal, which were internally connected to the ground reference of the module. This module was used to set the blower fan speed.

3.5 Measurement Procedures

3.5.1 Cross-wire Velocity Measurements

The straight cross-wire probe was mounted on the traversing system and inserted into the test section from the downstream end so that the sensor was at a distance of $x = 33.8D$ from the inlet of the test section (Figure 3.19), at an azimuthal angle $\phi = 180°$ and at a radial distance $r = 0.7D$ from the central rod (Figure 3.19). The probe was oriented with the use of a cathetometer so that it measured the streamwise and azimuthal velocity components. The data acquisition program was phase-locked to the motion of the linear actuator. The right-angled cross-wire probe was mounted in the port on the top cover of the test section located at $x/D = 33.7$. The hot-wire signals were corrected for temperature variation measured by an RTD that was positioned in the flow near the exit of the test section (see section 3.4.2). The hot-wire signals were low pass filtered at 14.3 kHz and sampled at a rate of 30 kHz. The RTD was sampled at 5 Hz. The hot-wire time series consisted of 3×10^5 samples. Following convergence analysis, data were collected and ensemble-averaged over 1500 cycles.

3.5.2 Time and Phase Averaging

Two types of averaging were used in this experiment: time averaging for the steady experiments and phase averaging for the unsteady experiments. Time averages, which are denoted by overbars, were computed as, for example,

$$\overline{U} = \int_0^{T_{av}} U(t)dt, \tag{3.21}$$

where the averaging time interval T_{av} was taken to be at least 100 integral time scales long (see definition of this scale in Section 3.7.4). Phase (or ensemble) averages, which are denoted by angle brackets, were computed as, for example,

$$< U(t) >= \frac{1}{N} \sum_{n=1}^{N} U_n(t), \tag{3.22}$$

where N is the total number of measurement cycles, equal to 1500 in this experiment.

Instantaneous velocity fluctuations for the calculation of turbulence statistics were computed by the application of Reynolds decomposition, as, for example,

$$u(t) = U(t) - \overline{U} \quad \text{or} \quad u(t) = U(t) - < U(t) > . \tag{3.23}$$

3.5.3 Cycle-to-cycle Variations

It was discovered that straightforward phase averaging of the turbulence measurements led to unrealistic results. This was attributed to strong cycle-to-cycle variations, which were particularly strong during deceleration. An example is shown in Figure 3.17, which clearly illustrates that velocity fluctuations u would be grossly overestimated, if they were calculated by subtracting the phase-averaged values $< U >$ from the instantaneous values U as mentioned in the previous section. To correct for cycle-to-cycle variation effects, the acceleration and deceleration parts of each cycle were fitted separately by least-squares fitting of a sigmoid-type curve. For the accelerating part of the cycle, this equation was

$$U_{sn,acc} = U_{low,acc} + \frac{U_{high,acc} - U_{low,acc}}{1 + e^{-k_{acc}(t_{acc} - t_{50,acc})}}, \tag{3.24}$$

where $U_{low,acc}$ is the lower velocity asymptote of the accelerating part, $U_{high,acc}$ is the upper velocity asymptote of the accelerating part, k_{acc} is the growth rate of the accelerating part, and $t_{50,acc}$ is the time at which the sigmoid curve reaches its middle value. $U_{low,acc}$ and $U_{high,acc}$ were specified, respectively, as the phase-averaged velocities one timestep (1/30000 s) before the beginning of the accelerating part of the curve (at $\Delta t = 0.4$s) and after the end of the accelerating part of the curve (at $\Delta t = 2.66$s). For the decelerating part of the cycle, the sigmoid equation was

$$U_{sn,dec} = U_{high,dec} - \frac{U_{high,dec} - U_{low,dec}}{(1 + e^{-k_{dec}(t_{dec} - t_{50,dec})})}, \tag{3.25}$$

where $U_{high,dec}$ is the higher velocity asymptote of the decelerating part, $U_{low,dec}$ is the lower velocity asymptote of the decelerating part, k_{dec} is the growth rate of the decelerating part, and $t_{50,dec}$ is the time at which the sigmoid curve reaches its middle value. $U_{low,dec}$ and $U_{high,dec}$ were specified, respectively, as the phase-averaged velocities one timestep (1/30000 s) before the beginning of the decelerating part of the curve (at $\Delta t = 3.66$s) and after the end of the decelerating part of the curve (at $\Delta t = 6.66$s). The values for k_{acc}, $t_{50,acc}$, k_{dec}, and $t_{50,dec}$ were determined via least-squares fitting with a MATLAB script. An example of the sigmoid fit is shown by the white line in Figure 3.17. The instantaneous value U_{sn} of the sigmoid curve for each cycle $n = 1, 2, ..., 1500$ was then used to compute the smoothed velocity fluctuations as

$$u_{sn}(t) = U_n(t) - U_{sn}(t),\ n = 1, 2, ..., 1500. \tag{3.26}$$

These fluctuations were then ensemble averaged to compute Reynolds stresses and length scales. It is evident that the smoothed fluctuations are smaller than the straightforward phase averages, as for example

$$< u_s^2 >=< u^2 > - < (U_s- < U >)^2 > . \tag{3.27}$$

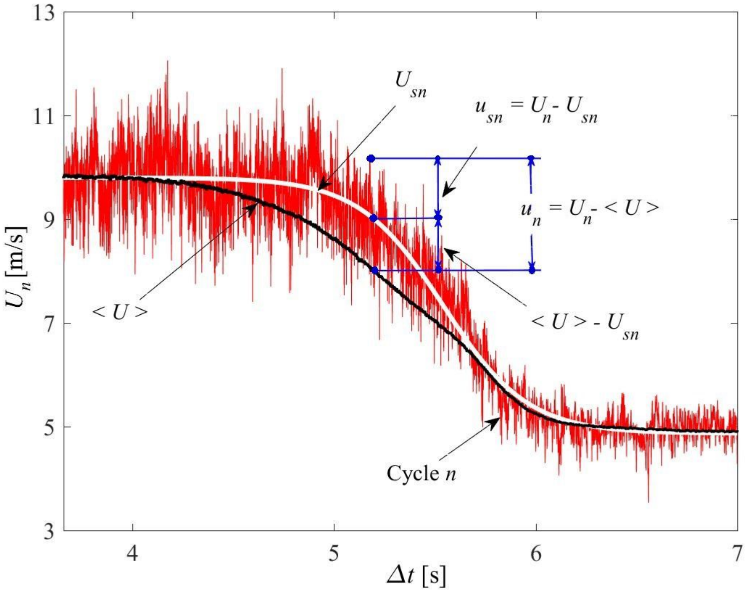

Figure 3.17: Comparison of ensemble-averaged velocity (black line) and velocity during an individual cycle (red line) during a time interval with decelerating flow. The sigmoid curve that was fitted to this cycle is also shown (white line).

All turbulence statistics for the unsteady flows were computed by using u_{sn}. For simplicity, however, we shall retain the symbol u when we refer to velocity fluctuations.

3.6 Velocity Measurement Uncertainty

The measurement uncertainty δ_X of a measured parameter X (for example, $< U_{gap} >$, $< u^2_{gap} >$, or $< (\partial u/\partial x)^2_{gap} >$) is defined as

$$\delta_X = \sqrt{b^2 + p^2} \ , \tag{3.28}$$

where b is the bias limit and p is the precision limit (Tavoularis, 2005). The portion of the total bias limit that was due to differences between calibration and measurement was estimated from Equation 3.19 to be approximately 0.5% of the measured quantity. This bias accounts for drifts in all instruments used and errors in calibration. Other types of bias that were considered were those introduced by sensor vibrations and possible probe misalignment with respect to the incoming flow.

All hot-wire probes and probe mounts were designed to keep the uncertainty as low as possible. The support of the straight cross-wire probe was mounted firmly on the traversing system, so that the effects of mechanical vibrations on the measured turbulence may be considered negligible. It is known that cross-wire probes may be subject to errors caused by cross-talk if they are spaced too closely to each other; however, Jerome et al. (1971) found that such errors would only be appreciable when the ratio of the separation distance to the length of the sensors is less than 0.15. This ratio was 0.5 for the two cross-wire probes used in this study.

The effect of the hot-wire probe misalignment with respect to the incoming flow on the mean flow velocity was studied on the calibration jet for pitch angles ranging from -3° to 3°. It was determined that, within this range, the measured mean flow velocity error ranged between 0.1 and 0.4%. It was estimated that when the probe was inserted in the test section, its axis formed an angle of less than 1° with the incoming flow and so the effect probe misalignment on the mean flow velocity was considered to be less than 0.3%.

The aluminium frames supporting the rods at the downstream end of the test section were at a considerable distance from the end of the test section and spaced out to keep flow blockage at the outlet at a low level. In addition, the hot-wire probe was inserted from the outlet fairly deep into the test section, so that blockage by the probe support and traversing systems would also be small.

The tip of the RTD probe used for temperature correction was at approximatively 20 mm downstream of the hot-wire so that thermal effects of the hot-wires on the RTD probe and aerodynamic effects of the RTD probe on the hot-wire measurements may be considered negligible.

The precision limit was calculated as

$$p = 2\sigma \ , \tag{3.29}$$

where σ is the standard deviation of the ensemble average of X.

The uncertainties of parameters that were determined by combining other measurements (e.g., the Taylor microscale and the Kolmogorov microscale) were estimated by standard statistical procedures (Tavoularis, 2005). Table 3.3 summarises the uncertainties of the measured and calculated parameters.

Table 3.3: Relative uncertainty estimates of measured properties.

Property	Lower Bound (%)	Upper Bound (%)
$< U_{gap} >$	2.8	7.4
$< U_{CS} >$	2.0	6.1
$< u^2_{gap} >$	7.2	11.0
$< u^2_{CS} >$	6.2	9.6
$< (\partial u/\partial x)^2_{gap} >$	8.4	14.6
$< (\partial u/\partial x)^2_{CS} >$	6.6	10.2
λ_{gap}	6.5	10.5
λ_{CS}	5.6	9.4
η_{gap}	0.2	0.7
η_{CS}	0.2	0.6

3.7 Definitions

3.7.1 Rod-bundle Geometry and Coordinate System

A model of a sector of the CANDU 37-rod bundle was used in this study. Our interest focuses in the middle of the central rod-wall gap and in the middle of the central outer subchannel (Figure 3.18).

The cylindrical coordinate system (x, r, ϕ) that was used in this study is shown in Figure 3.19. The x-axis ("axial" direction) is along the axis of the central rod and has its origin on the upstream side of the endplate that holds the test section at its inlet; the r-direction ("radial" one) is along a central rod radius and the ϕ-direction ("azimuthal" one) is circumferential to the central rod.

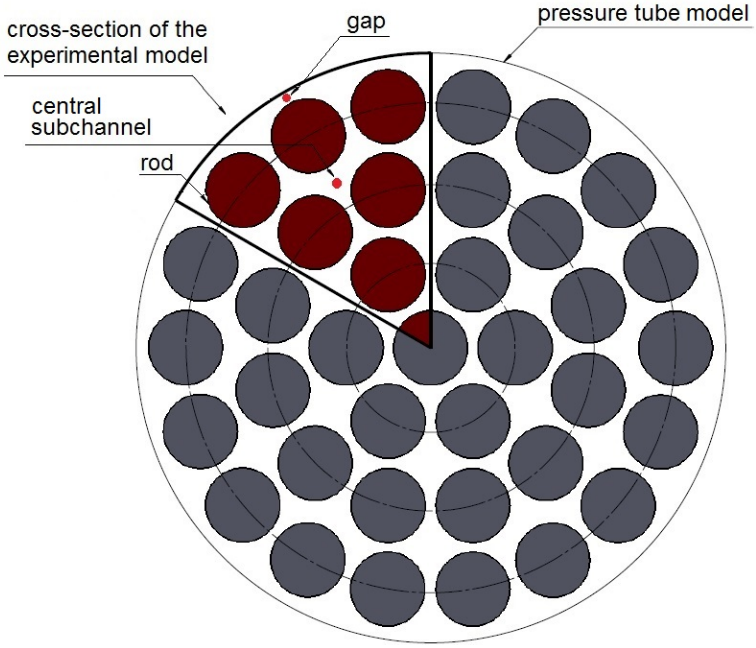

Figure 3.18: Cross-section of a CANDU 37-rod bundle (Don, 2016).

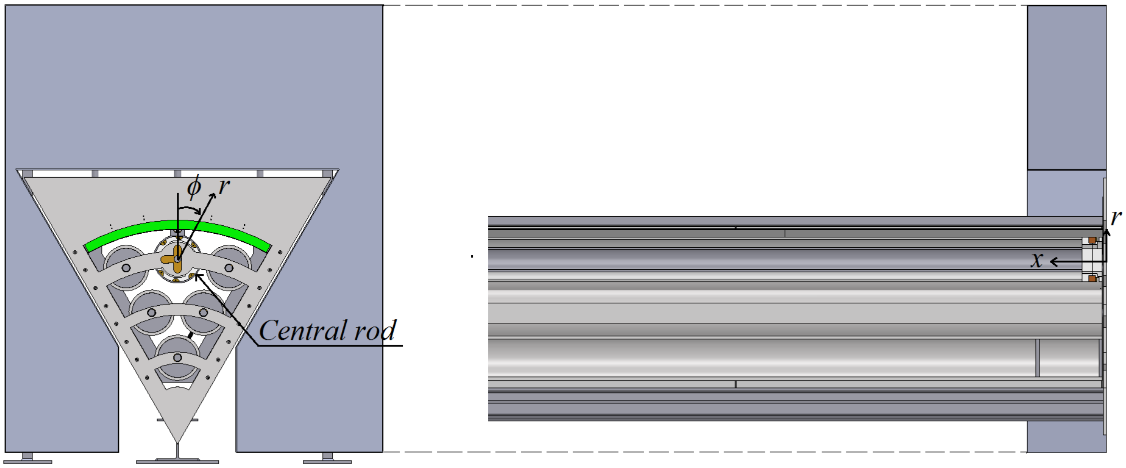

Figure 3.19: Downstream view (left) and side view (right) of the test section, showing the coordinate system.

3.7.2 Hydraulic Diameter

The hydraulic diameter, D_h, is the diameter of a pipe that has approximately equal pressure loss as a non-circular duct or open channel. It is defined as

$$D_h = \frac{4A_c}{P_c}, \tag{3.30}$$

where A_c is the cross-sectional area of the duct and P_c is the wetted perimeter of the cross-section.

A full CANDU 37-rod bundle, shown in Figure 3.18, has a hydraulic diameter

$$D_{h_{CANDU}} = \frac{\pi(4R_T^2 - 37D^2)}{2\pi R_T + 37\pi D}, \tag{3.31}$$

where R_T is the radius of the pressure tube and D is the diameter of the rods. As seen in Figure 3.19, the experimental model is a 60° section of the CANDU 37-rod bundle. It consists of six full rods and one-sixth segment of a rod. It also has two plane side walls, which are not present in the full rod-bundle. The cross-sectional area and wetted perimeter for the model were calculated as

$$A_t = \frac{\pi(4R_T^2 - 37D^2)}{24}, \tag{3.32}$$

and

$$P_t = \frac{(2\pi + 12)R_T + (37\pi - 6)D}{6}, \tag{3.33}$$

from which one can calculate the hydraulic diameter as

$$D_{h_{model}} = \frac{\pi(4R_T^2 - 37D^2)}{(2\pi + 12)R_T + (37\pi - 6)D}. \tag{3.34}$$

The values of the hydraulic diameters of the CANDU 37-rod bundle, the upscaled model and the experimental model itself were, respectively, 7.4 mm, 95.2 mm and 73.6 mm (Table 3.4). The presence of the side walls makes the hydraulic diameter of the experimental model significantly smaller than that of a full rod bundle.

Table 3.4: Specifications of an actual CANDU rod bundle, 12.9:1 37-rod bundle and the experimental model.

	CANDU rod bundle	Large-scale 37-rod bundle	Experimental model
Scale	1:1	12.9:1	12.9:1
Configuration	full bundle	full bundle	1/6 of a full bundle with side walls
Number of rods	37	37	6+1/6
D (mm)	13.08	168.73	168.73
R_T (mm)	51.69	666.80	666.80
D_h (mm)	7.4	95.2	73.6

3.7.3 Reynolds and Strouhal Numbers

The bulk velocity U_b in this experiment was defined as

$$U_b = \frac{Q}{A_t}, \tag{3.35}$$

where Q is the volumetric flow rate and A_t is the cross-sectional area of the test section. A procedure on determining the bulk velocity is described in Section 3.2 of the thesis by Don (2016).

In this study, two Reynolds numbers were used; the bulk Reynolds number and the local Reynolds number. The bulk Reynolds number, which was used in the first part of the experiment, was defined as

$$\mathrm{Re}_b \ = \frac{\rho U_b D_h}{\mu}. \tag{3.36}$$

The local Reynolds number, which was used in the second part of the experiment, was defined as

$$\mathrm{Re} \ = \frac{\rho < U > D_h}{\mu}, \tag{3.37}$$

where $< U >$ is the instantaneous local phase-averaged velocity.

The Strouhal number of the vortex street, which is a dimensionless frequency, was defined as

$$\mathrm{St} \ = \frac{fD}{U_b}, \tag{3.38}$$

where f is the instantaneous frequency of the vortex street.

3.7.4 Turbulence Properties

As mentioned previously, velocity fluctuations in each cycle were estimated as differences between the instantaneous values and corresponding smoothed velocity time series, which resulted in a significant reduction of errors introduced by cycle-to-cycle variations. For simplicity of notation, in the remainder of the thesis we will drop the subscript s from corrected properties; for example, the symbol $< u^2 >$ will be used instead of $< u_s^2 >$. The following definitions were applied to these (*i.e.*, corrected) fluctuations.

First, the normal Reynolds stresses per unit mass $< u^2 >$, $< u_r^2 >$ and $< u_\phi^2 >$, which are, respectively, the variances of the axial, radial and azimuthal velocity fluctuations, were calculated and then the turbulent kinetic energy per unit mass was computed as

$$k = \frac{1}{2}(< u^2 > + < u_r^2 > + < u_\phi^2 >). \tag{3.39}$$

For steady flows, time averages were used instead of phase averages.

A general definition of the autocorrelation coefficient of the streamwise velocity fluctuations is

$$R(t,\tau) = \frac{< u(t)u(t+\tau) >}{(< u^2(t) >< u^2(t+\tau) >))^{1/2}}. \tag{3.40}$$

A streamwise integral time scale may be calculated by integrating the corresponding autocorrelation coefficient to its first zero crossing τ_0, namely as

$$T(t) = \int_t^{t+\tau_0} R(t,\tau)d\tau. \tag{3.41}$$

For stationary random processes, for which statistical properties are independent of shifts in time origin, these definitions may be simplified to

$$R(\tau) = \frac{< u(0)u(\tau) >}{< u^2(0) >}, \tag{3.42}$$

and

$$T = \int_0^{\tau_0} R(\tau)d\tau. \tag{3.43}$$

The integral length scale represents the average size of the most energetic eddies in a turbulent flow. The streamwise integral length scale was calculated with the use of Taylor's frozen flow approximation as

$$L(t) =< U(t) > T(t). \tag{3.44}$$

The streamwise Taylor microscale was computed as

$$\lambda(t) =< U(t) > \sqrt{\frac{< u^2 >}{< (\partial u/\partial t)^2 >}}\ , \tag{3.45}$$

from which the streamwise turbulence Reynolds number was determined as

$$\mathrm{Re}_\lambda(t) = \frac{\rho < u^2 >^{1/2} \lambda}{\mu} \quad . \tag{3.46}$$

The turbulent kinetic energy dissipation rate per unit mass was estimated from the isotropic expression (Pope, 2001)

$$\epsilon(t) = 15\nu \frac{< u^2 >}{\lambda^2(t)}. \tag{3.47}$$

The Kolmogorov microscale, which represents the size of the smallest dynamically significant eddies in turbulent flows, was determined as

$$\eta(t) = \left(\frac{\nu^3}{\epsilon(t)}\right)^{1/4}. \tag{3.48}$$

Finally, the dissipation parameter (Nedić et al., 2017) was determined as

$$C_\epsilon(t) = L(t) \frac{\epsilon(t)}{< u^2 >^{3/2}}. \tag{3.49}$$

3.7.5 Gap Vortex Street Frequency

Coherent structures are interconnected, large-scale structures that have phase correlated vorticity and which cause transport of momentum across a certain distance (El Tahry, 1990; Hussain, 1983). They are regions within the flow, where at a given time, the turbulent quantities such as velocity, vorticity, pressure density or temperature tend to remain unaffected by the random motion of the flow (Lesieur, 1997). In tightly-packed rod bundles, coherent structures in the form of vortex streets, cause strong momentum and mass transfer across the narrow gaps. This results in an increase of the local heat transfer coefficient, improving the thermalhydraulic performance. Because of the non-stationary nature of the present flow, spectral analysis cannot be used for determining the frequency of vortex streets. Instead, a wavelet transform, which allows the determination of the frequency at each time during the cycle, was used.

A wavelet is a wave-like oscillation. Wavelets are used in time-frequency analysis of signals, particularly for the identification of frequencies with significant energy in non-stationary signals (Tavoularis, 2005). The most commonly used wavelet for time-frequency analysis of signals is the Morlet wavelet. It is defined as

$$\psi(\tau) = \pi^{\frac{1}{4}} e^{j2\pi\gamma_0\tau} e^{\frac{-\tau^2}{2}}, \tag{3.50}$$

where $j = \sqrt{-1}, \tau$ is a dimensionless variable and γ_0 is the dimensionless centre frequency of the wavelet.

The gap vortex street frequency was determined by analysing the signals of a right-angled cross-wire probe, positioned at mid-gap. As part of a simplified calibration procedure, this probe was positioned in the calibration jet with its axis aligned with the jet axis and the jet speed was varied within the range of interest. The DC offset and the gain of each anemometer module were repeatedly adjusted until the mean difference between the output voltages of the two probe sensors became insensitive to changes in the streamwise velocity, which made this voltage difference an approximately linear function of the transverse velocity fluctuation. By following this procedure, we avoided the need for performing a more elaborate, angular cross-wire probe calibration.

Using the Morlet wavelet in the MATLAB signal analysis package, the time-frequency plots were determined by fitting the Morlet wavelet to the difference of the signals of the two probes. This signal was essentially proportional to the azimuthal velocity fluctuation at mid-gap, which is a very sensitive indicator of the passage of vortices. Once fitted, the MATLAB signal analysis program determined the best-fitted frequency during each cycle, which was phase averaged over 1500 cycles. An example of the results of the wavelet analysis for one cycle is shown in Figure 3.20.

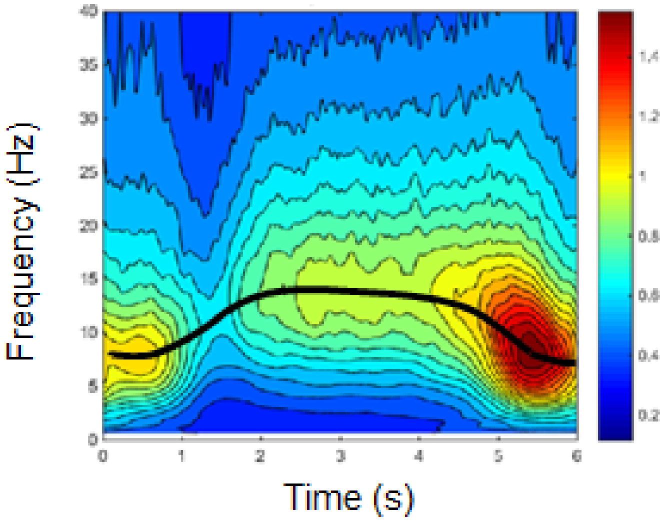

Figure 3.20: Wavelet map during a representative cycle. Solid line indicates the best estimate of the time-dependent frequency variation.

Chapter 4

Experimental Results and Discussion

4.1 Steady Flow Measurements

4.1.1 A Test of the Effect of the Flap Position

Steady flow measurements of the mean velocity, the normal and two shear Reynolds stresses, the turbulent kinetic energy, the streamwise integral length scale, the Taylor and Kolmogorov microscales and power spectra were reported by Don (2016) in the same facility before the installation of the bypass branch. Such measurements were taken at three bulk Reynolds numbers, namely $\mathrm{Re}_b = 50\ 000$, 100 000, and 130 000. In order to detect any possible effect of the position of the flap on the flow and turbulence distributions, similar measurements were taken along a radial direction on the axis of symmetry in the central subchannel at $\mathrm{Re} = 69\ 000$ for two different bypass conditions, shown schematically in Figure 4.1. In the first condition, the flap was in a fully closed position and the bypass branch exit was sealed. In the second condition, the flap was at a half-way position, the bypass branch exit was fully open, and the speed of the blower was increased to produce the same bulk Reynolds number as in the first condition.

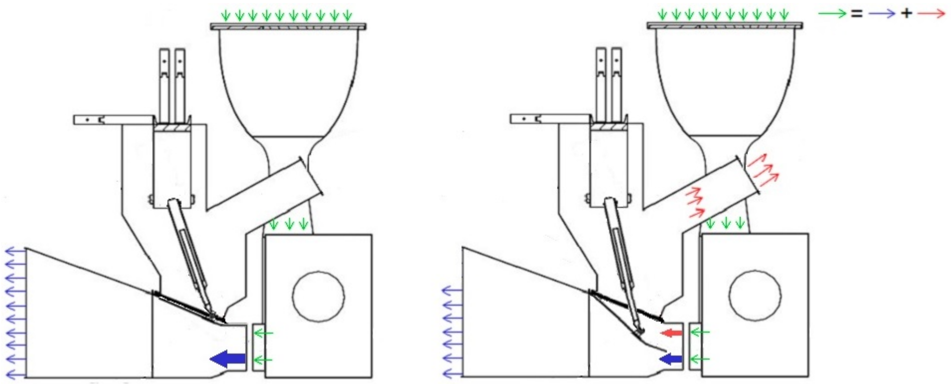

Figure 4.1: Fully closed position of flap and sealed bypass branch (left). Half-open position of bypass flap and open bypass branch (right).

Representative radial profiles of mean and turbulence properties along the axis of symmetry in the central subchannel ($\phi = 180°$) for the two bypass branch conditions are shown in Figures 4.2 to 4.10. The bulk Reynolds number was 69,000 in all cases. Differences between corresponding profiles were relatively small and could be attributed in part to small mismatches of bulk velocity, calibration drift, misalignment of probes and other experimental errors. We may then conclude that for a fixed bulk Reynolds number, the position of the flap has a relatively small, if any, effect on the flow in the test section.

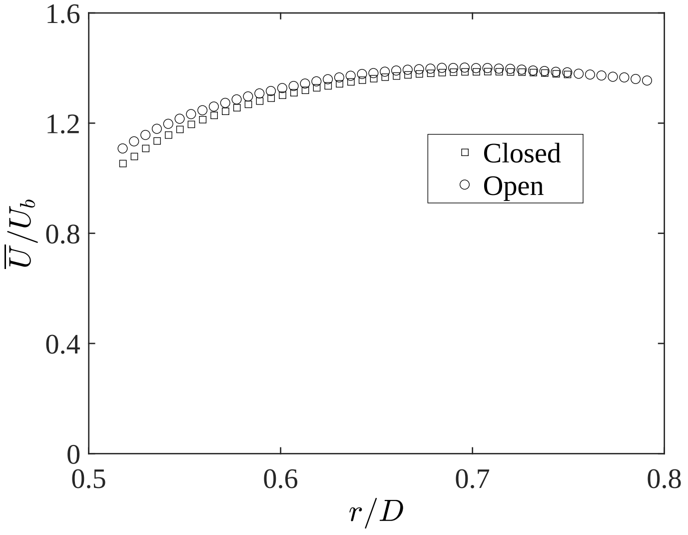

Figure 4.2: Comparison of axial velocity radial profiles for steady flow with two bypass branch conditions.

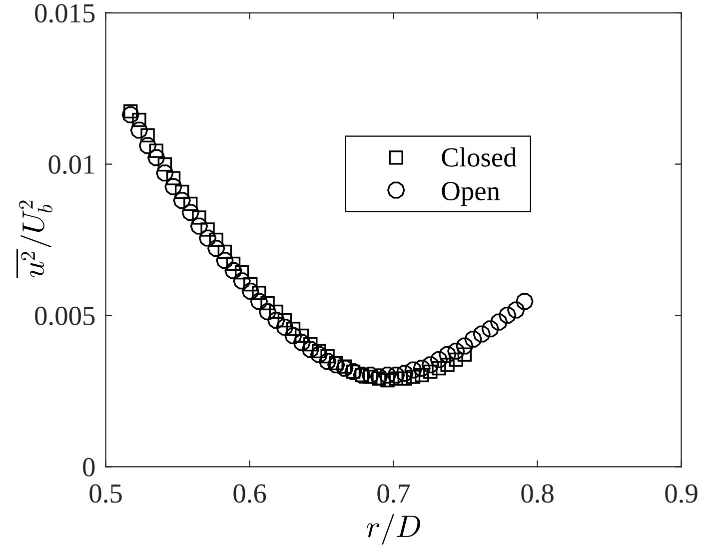

Figure 4.3: Comparison of streamwise Reynolds stress radial profiles for steady flow with two bypass branch conditions.

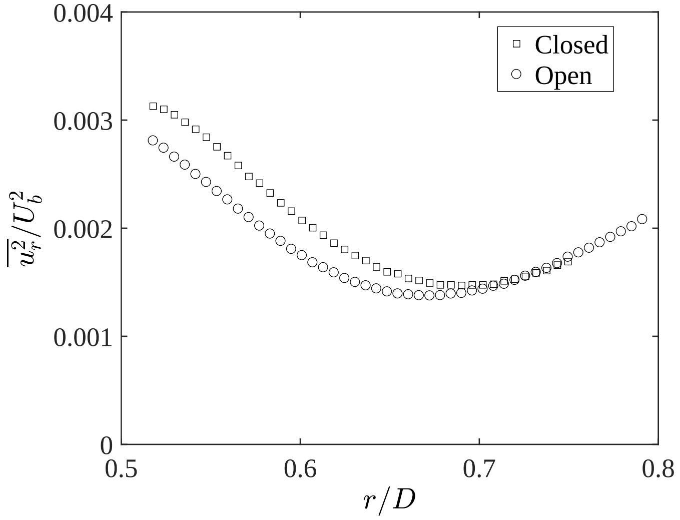

Figure 4.4: Comparison of radial Reynolds stress radial profiles for steady flow with two bypass branch conditions.

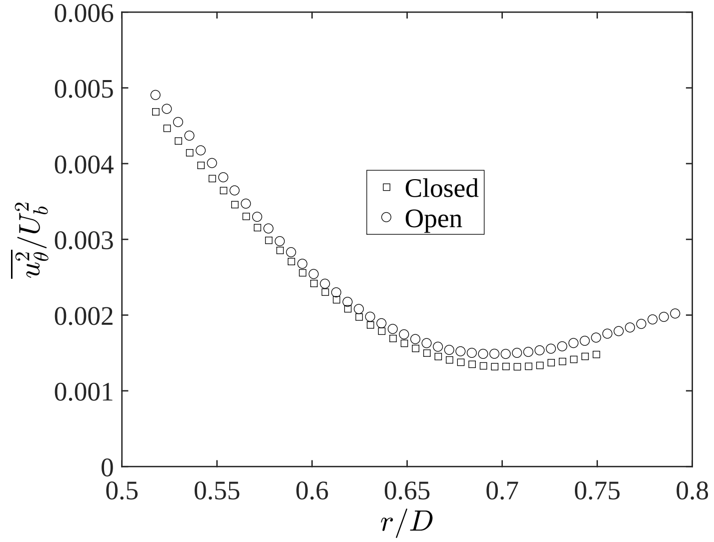

Figure 4.5: Comparison of azimuthal Reynolds stress radial profiles for steady flow with two bypass branch conditions.

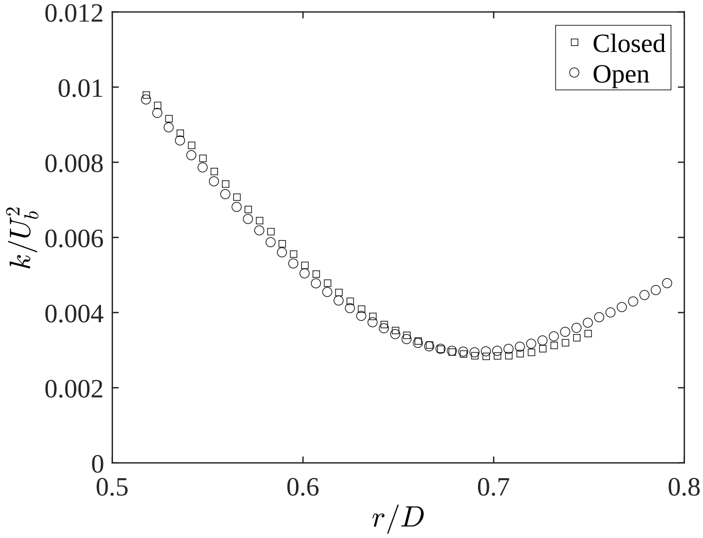

Figure 4.6: Comparison of turbulent kinetic energy radial profiles for steady flow with two bypass branch conditions.

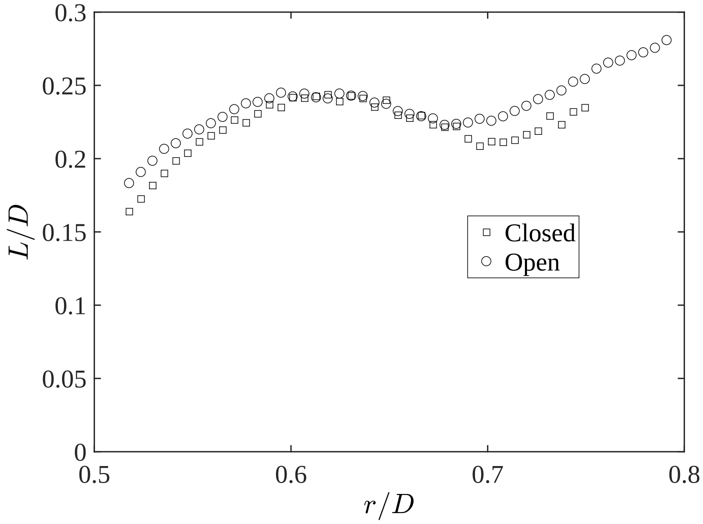

Figure 4.7: Comparison of integral length scale radial profiles for steady flow with two bypass branch conditions.

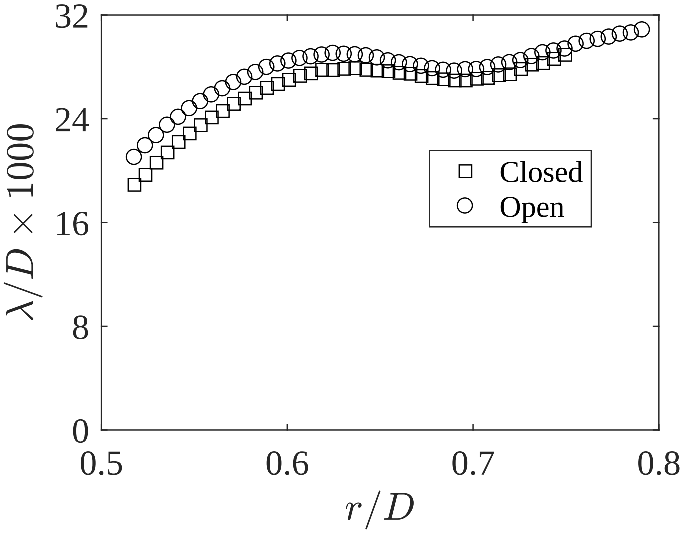

Figure 4.8: Comparison of Taylor microscale radial profiles for steady flow with two bypass branch conditions.

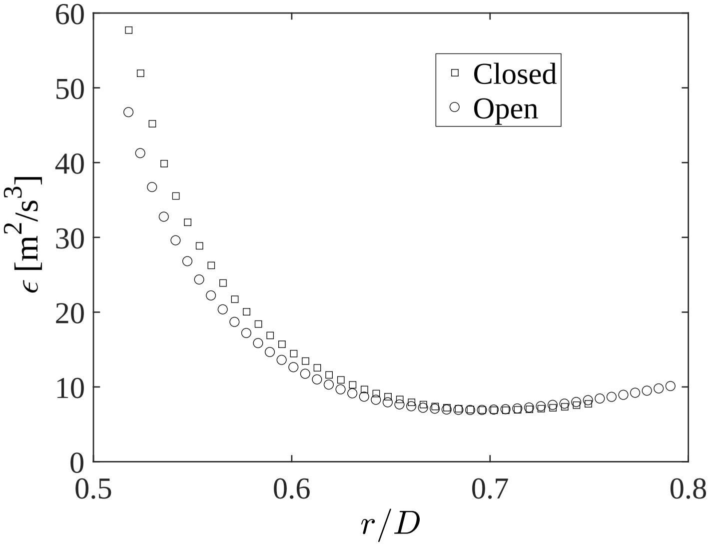

Figure 4.9: Comparison of dissipation rate radial profiles for steady flow with two bypass branch conditions.

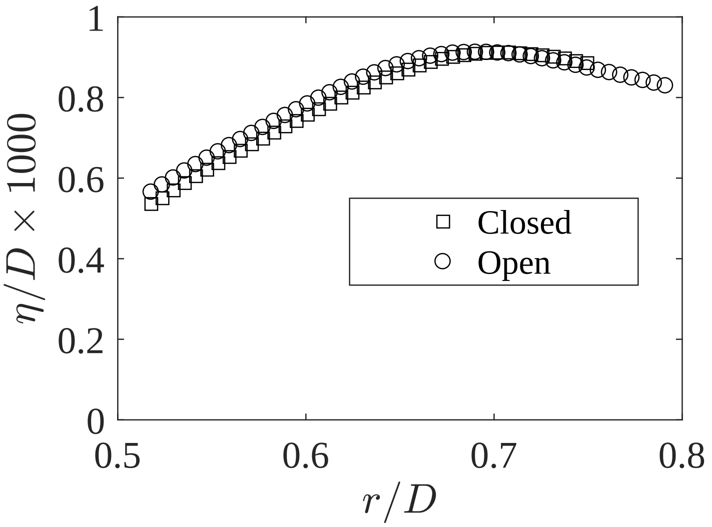

Figure 4.10: Comparison of Kolmogorov microscale radial profiles for steady flow with two bypass branch conditions.

4.1.2 Reference Steady Flow Measurements

The transient flow measurements will be discussed by comparison to corresponding steady flow measurements at the same Reynolds number. To construct a steady-flow reference database, a full set of measurements were collected at mid-gap and in the centre of the central subchannel for each of six Reynolds numbers within the range of values of the transient tests. Some measured values for these results are shown in Table 4.1. Corresponding steady-flow values for each transient flow velocity were found by interpolation. The steady flow measurements will be plotted together with the corresponding transient results.

Table 4.1: Reference steady flow properties.

Re_b	21 600	31 200	34 200	36 400	38 000	39 800
Re_{gap}	22 400	33 700	39 000	41 500	43 000	45 500
Re_{CS}	31 900	46 500	53 000	56 000	58 500	61 000
$\mathrm{Re}_{gap}/\mathrm{Re}_{CS}$	0.702	0.725	0.736	0.741	0.735	0.746
$\mathrm{Re}_{CS}/\mathrm{Re}_b$	1.48	1.49	1.55	1.54	1.54	1.53
$\overline{u^2{}_{gap}}$ $[\mathrm{m}^2/\mathrm{s}^2]$	0.088	0.173	0.226	0.264	0.298	0.333
$\overline{u^2_{CS}}$ $[\mathrm{m}^2/\mathrm{s}^2]$	0.095	0.180	0.221	0.245	0.264	0.293
L_{gap}/D	0.553	0.554	0.425	0.459	0.469	0.358
L_{CS}/D	0.614	0.841	0.503	0.577	0.594	0.649
$\lambda_{gap}/D \times 1000$	22.9	20.6	19.6	19.2	19.1	18.9
$\lambda_{CS}/D \times 1000$	31.0	27.9	25.9	25.6	25.8	25.1
ϵ_{gap} $[\mathrm{m}^2/\mathrm{s}^3]$	1.00	3.75	5.08	5.82	6.31	6.91
ϵ_{CS} $[\mathrm{m}^2/\mathrm{s}^3]$	0.80	1.88	2.67	3.03	3.21	3.63
$\eta_{gap}/D \times 1000$	1.28	1.05	0.97	0.94	0.92	0.90
$\eta_{CS}/D \times 1000$	1.54	1.24	1.14	1.10	1.09	1.06

4.2 Transient Flow Results

4.2.1 Phase-averaged Velocity

Velocity measurements were taken with cross-wire probes, oriented such that they measured simultaneously the instantaneous axial and azimuthal velocity components. One probe was positioned in the centre of the rod-wall gap ($\phi = 0°$) and another in the central subchannel, at $r = 0.70D$ on the axis of symmetry of the test section ($\phi = 180°$).

The period of each cycle was 7.00 s. As shown in Figure 4.11, each cycle was subdivided into four distinct intervals:

- a steady-flow interval at a relatively low velocity for $0.00 \text{ s} \leq \Delta t \leq 0.40 \text{ s}$ and $6.66 \text{ s} \leq \Delta t \leq 7.00 \text{ s}$,
- an accelerating flow interval for $0.40 \text{ s} < \Delta t < 2.66 \text{ s}$,
- a steady-flow interval at a relatively high velocity for $2.66 \text{ s} \leq \Delta t \leq 3.66 \text{ s}$,
- a decelerating flow interval for $3.66 \text{ s} < \Delta t < 6.66 \text{ s}$.

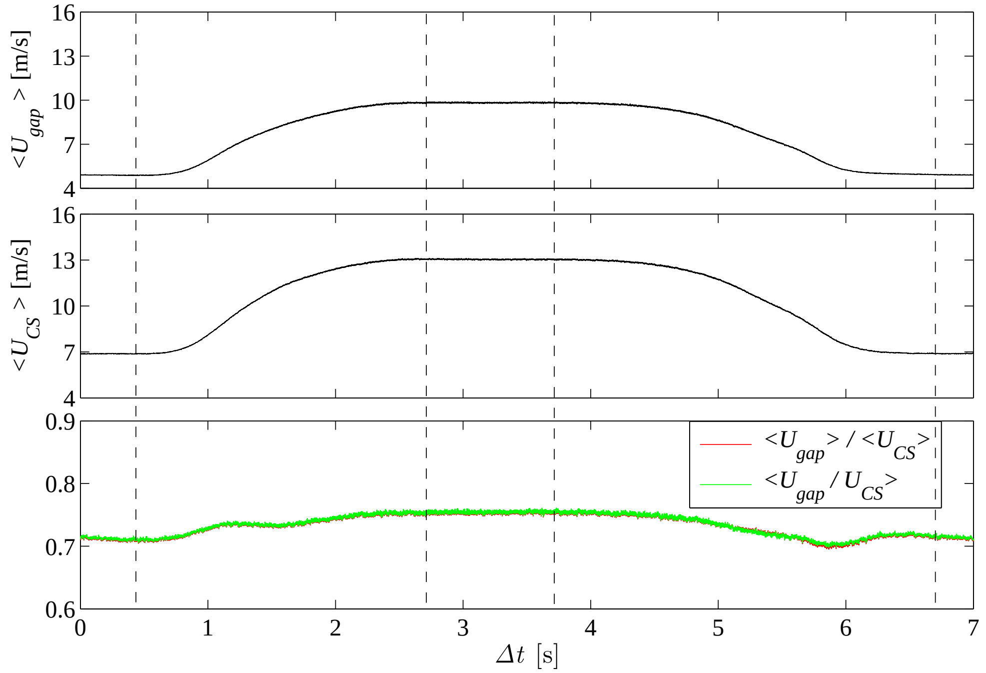

Figure 4.11: Plots of the phase-averaged axial velocities in the gap (top) and the central (middle) subchannel, as well as their ratios (bottom). Dashed lines separate intervals with steady, accelerating and decelerating flows.

In the present experiments, the time intervals during which strong acceleration or deceleration occurred were roughly 2 s. Such settings are relevant to nuclear reactor transient operation and it can be expected that the present transient results will show measurable differences from corresponding steady-flow results. Transient intervals in previous experimental studies of reactor systems were comparable in length, or even longer. For example, transient intervals were roughly 4-5 s long in the experiments of Zhang et al. (2011) and Chen et al. (2005) and about 10 s long in the experiments of Chun et al. (2009) and Watanabe et al. (2011).

The ratio of the phase-averaged velocities at the gap and the central subchannel and the corresponding phase-averaged instantaneous ratio are also shown in Figure 4.11. The fact that the two ratios essentially coincided during the entire cycle indicates that there was no peculiar correlation between cycle-to-cycle variations at the two locations. The value of these ratios was measurably larger during the high-speed steady-flow interval than during the low-speed one, which is compatible with the expectation that the flow distribution in the rod bundle would tend to become more uniform as the Reynolds number increases and the boundary layers become thinner.

For a meaningful comparison between transient and corresponding steady results, it seems most appropriate that the instantaneous bulk Reynolds numbers should be matched. Because of the absence of measurements of this property during the cycle, this can only be done approximately. Noticing that, during steady flow, the ratio $\mathrm{Re}_{CS}/\mathrm{Re}_b$ is insensitive to Re_b, we will assume that the value of this ratio was the same for both steady and transient flows, and so we will estimate transient Re_b from the measured Re_{CS}. For example, for the instant with $\Delta t = 1.5$ s, which was at mid-acceleration, $< U_{CS} >= 10.96$ m/s. For steady flow, this corresponds to $U_b = 7.26$ m/s, or $\mathrm{Re}_b = 34\ 700$, and we will assume that the latter value applies to the transient as well. Although there is a measureable effect of Reynolds number on the gap velocity, the effect is small in the central subchannel because the flow rate through the gap region is much smaller than in the central subchannel, which provides some justification for the previous assumption.

4.2.2 Vortex Street Frequency

The phase-averaged frequency of the vortex street across the rod-wall gap, determined by applying the Morlet wavelet transform to the corresponding transverse velocity signal, is shown in Figure 4.12. It is well known that, in fully turbulent, steady, rod-bundle flows, this frequency is nearly proportional to the Reynolds number and its value has been correlated with the efficiency of inter-subchannel flow mixing. Accordingly, the Strouhal number, St, of steady vortex streets is insensitive to mild changes of the Reynolds number. Figure 4.13 is a comparison of values of this Strouhal number for different values of the estimated bulk Reynolds numbers during steady, accelerating and decelerating time intervals. It can be seen that in all cases the Re-effect was quite weak and so was the unsteadiness effect. One may discern, however, that by comparison to steady flows at the same Re, accelerating flows had a 2-3% higher St and decelerating flows had a 2-3% lower one.

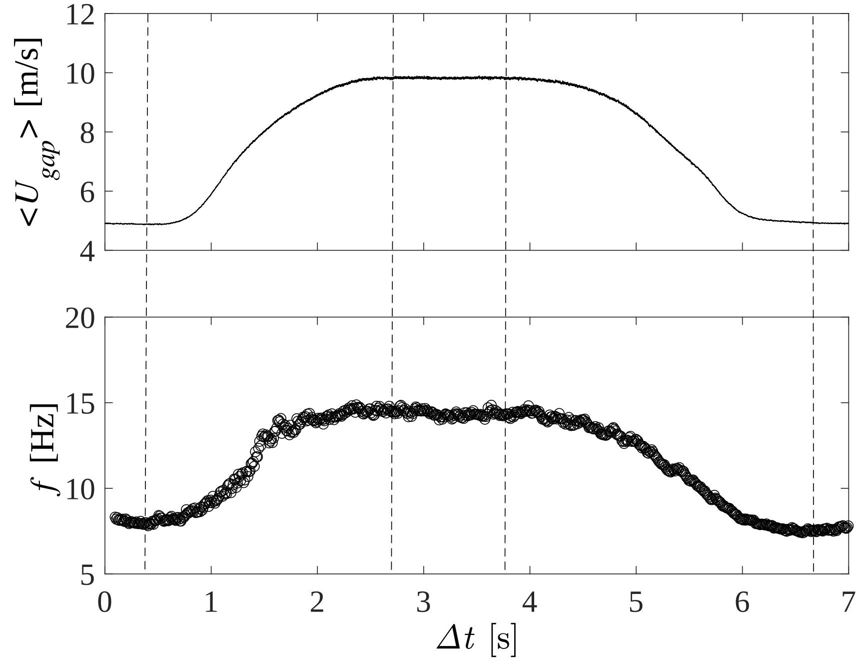

Figure 4.12: Vortex street frequency variation during the cycle.

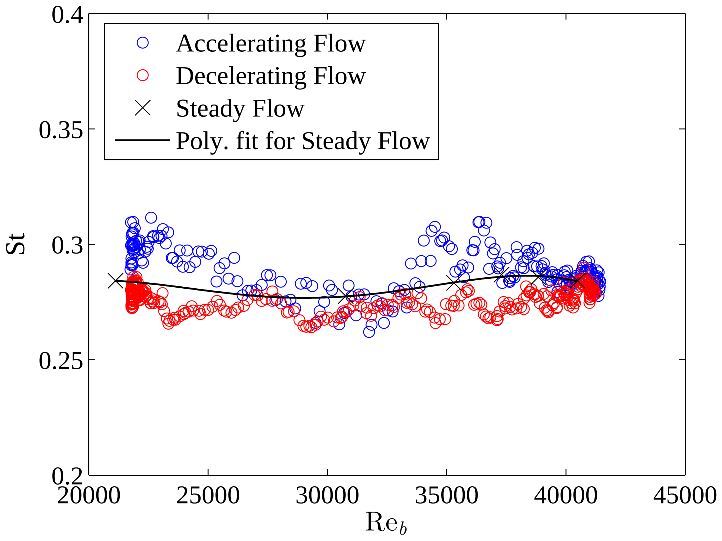

Figure 4.13: Comparison of the vortex street Strouhal numbers for accelerating, decelerating and steady flows.

4.2.3 Axial Velocity Fluctuations

As explained in Section 3.5.3, the calculation of turbulent fluctuations from Reynolds decomposition provided erroneous results because of the effects of cycle-to-cycle variation. In an effort to reduce such errors, instantaneous turbulent fluctuations were computed with reference to a smooth sigmoid curve that was fitted to each cycle. As shown in Figure 4.14, the difference between corrected and uncorrected values of the axial velocity variance was very large during the decelerating flow interval, but hardly visible during the steady and accelerating flow intervals.

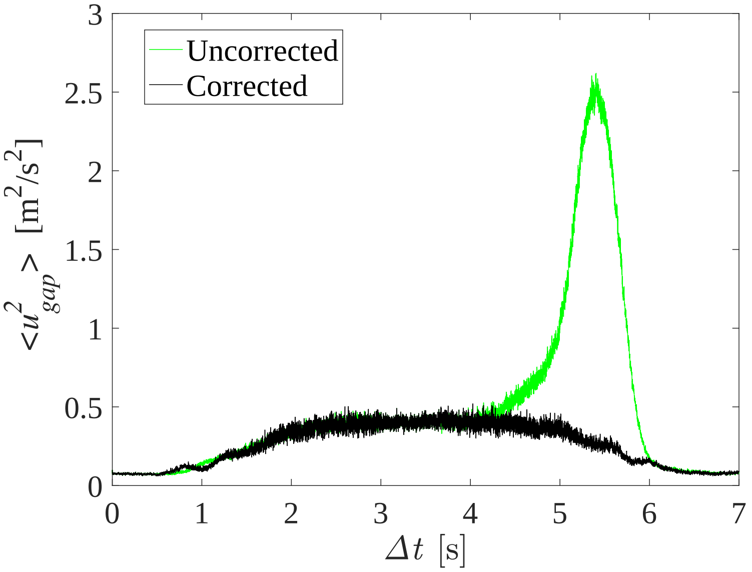

Figure 4.14: Uncorrected (green) and corrected (black) variances of the axial velocity fluctuations in the gap; comparable correction levels were also observed for the axial velocity in the central subchannel .

Figure 4.15 shows the variance of the corrected axial velocity fluctuations during the cycle in both the gap and the central subchannel, as well as the corresponding local turbulence intensities. Some possible residual errors are visible in the plots during the accelerating and decelerating portions of the flow. The effect of acceleration and deceleration on the local turbulence intensity is rather unclear and does not appear to be consistent at the two measuring locations.

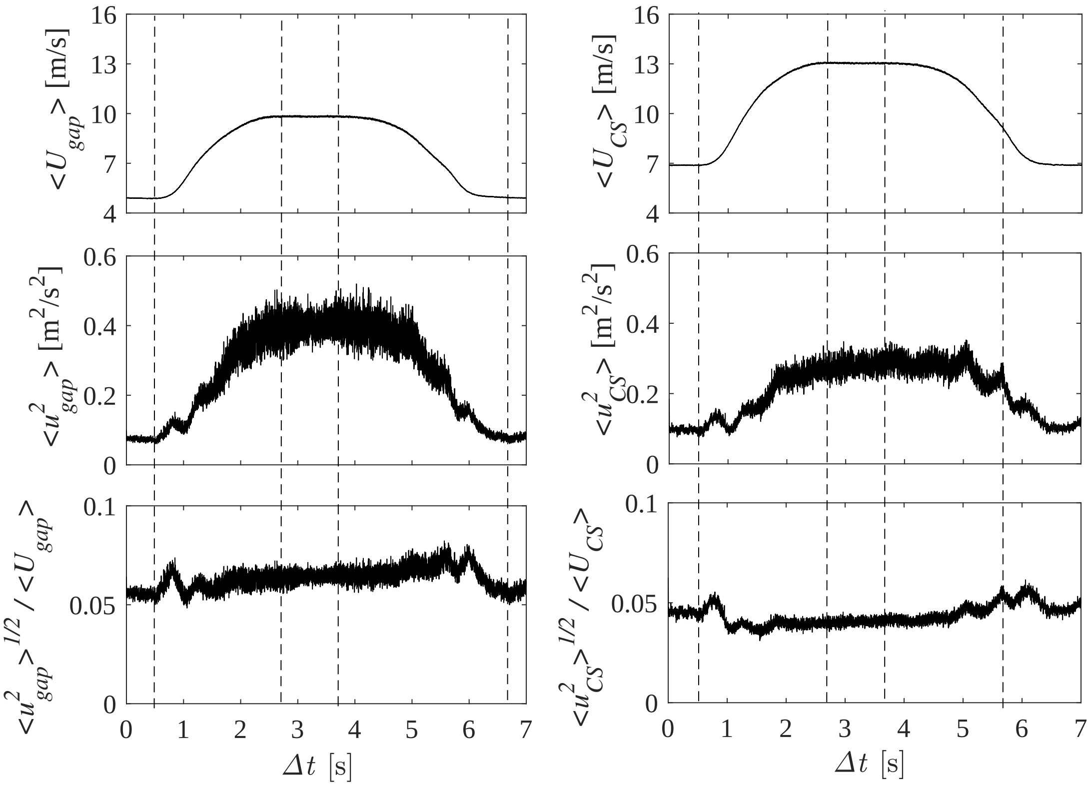

Figure 4.15: Temporal variations of axial velocity variances and local turbulence intensities at mid-gap (left) and in the central subchannel (right).

The transient and steady axial turbulence intensity (standard deviation normalised by the bulk velocity) at the two measuring locations within the range of equivalent Reynolds numbers are shown in Figure 4.16. At both locations, the values for accelerating flows are on the whole lower than those in steady flows, whereas the decelerating flow values are measurably higher than the steady ones. These observations are generally consistent with the expectation that acceleration tends to reduce the turbulence level and deceleration tends to increase it.

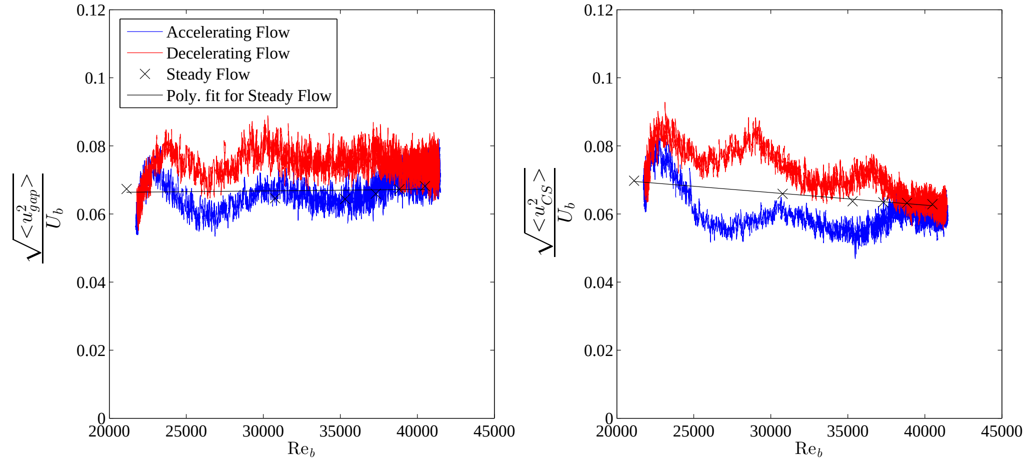

Figure 4.16: Turbulence intensities for accelerating, decelerating and steady flows at mid-gap (left) and in the central subchannel (right).

4.2.4 Autocorrelation Coefficient and Integral Length Scale

The uncorrected autocorrelation coefficient of the axial velocity, defined in Section 3.42, crossed zero when measurements were taken during the steady part of the flow, but remained positive during the accelerating and decelerating parts of the flow. This is shown in Figures 4.17 to 4.20 for the mid-gap location, but it was also true for the central subchannel. This prevented us from calculating the integral length scale. When, however, the fluctuations were taken with respect to the smoothed velocity, the autocorrelation coefficient crossed zero within 1 s for all cases and the integral length scale could be calculated.

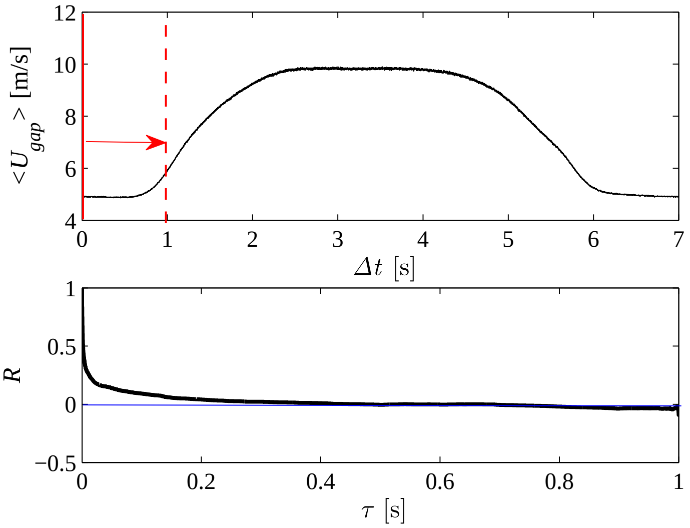

Figure 4.17: Autocorrelation coefficient of the axial velocity at mid-gap for $\Delta t = 0.002$s; the range of τ is bounded by the solid and dashed red lines.

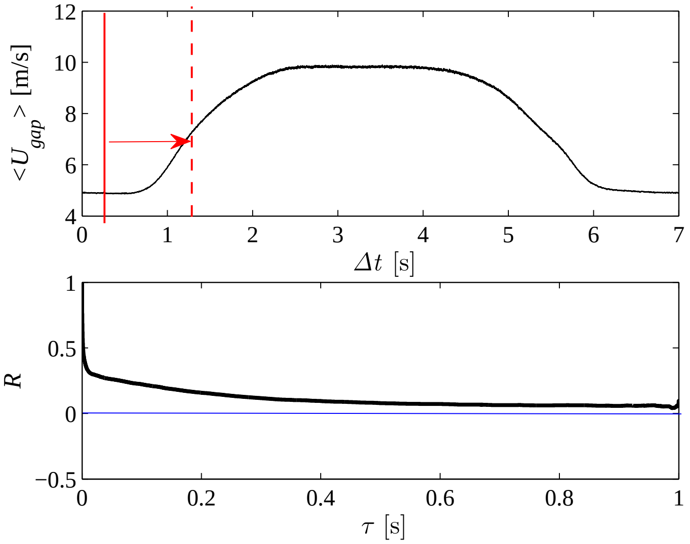

Figure 4.18: Autocorrelation coefficient of the axial velocity at mid-gap for $\Delta t = 0.202$s; the range of τ is bounded by the solid and dashed red lines.

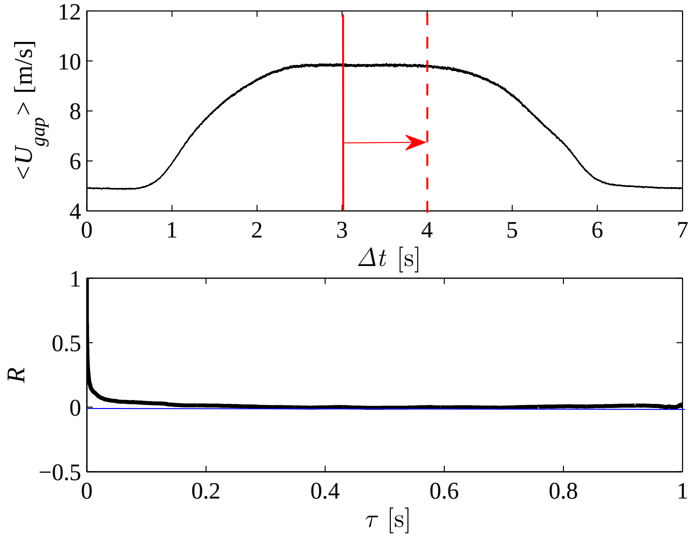

Figure 4.19: Autocorrelation coefficient of the axial velocity at mid-gap for $\Delta t = 3.002$s; the range of τ is bounded by the solid and dashed red lines.

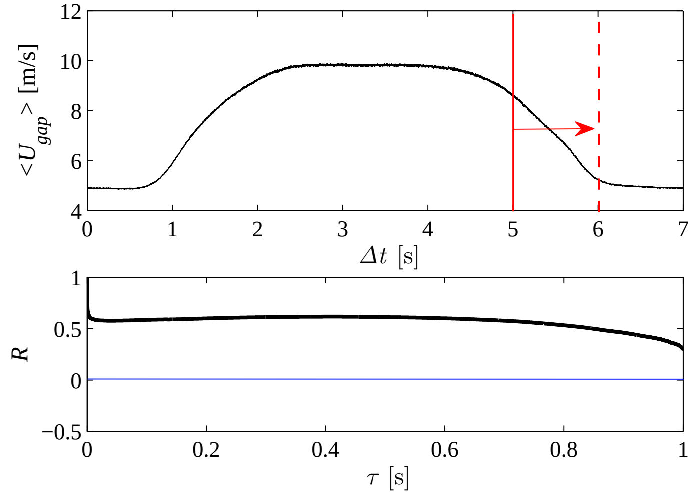

Figure 4.20: Autocorrelation coefficient of the axial velocity at mid-gap for $\Delta t = 5.002$s; the range of τ is bounded by the solid and dashed red lines.

Figure 4.21 shows that, both during acceleration and during deceleration, the integral length scales became as large as two times the corresponding steady value at mid-gap and up to four times the steady value in the central subchannel. Despite the relatively large scatter in the data, such differences are too large to be attributed to experimental errors alone. The same observations can be made for Figure 4.22.

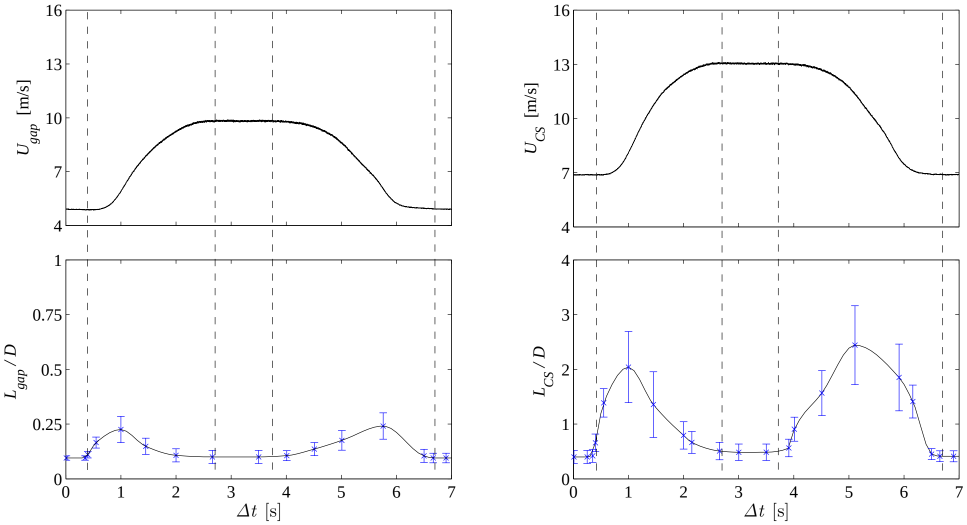

Figure 4.21: Integral length scale of the axial velocity at mid-gap (left) and in the central subchannel (right) during the cycle.

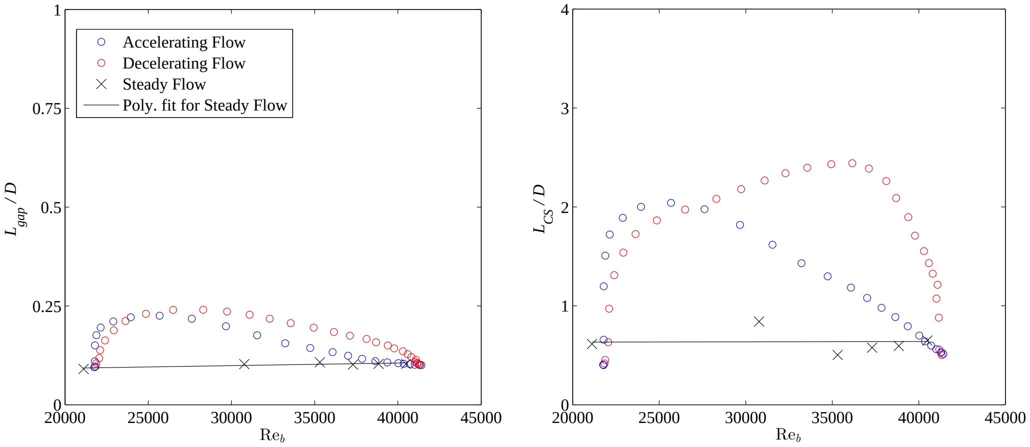

Figure 4.22: Comparison of integral length scale of the axial velocity at mid-gap (left) and in the central subchannel (right) for steady, accelerating and decelerating flows.

4.2.5 Taylor Microscale and Turbulent Reynolds Number

The variation of the Taylor microscale, normalized with the rod diameter, in the gap and the central subchannel during the cycle is plotted in Figure 4.23. The values in the low-speed steady-flow interval were measurably larger than those in the high-speed steady-flow interval. This is attributed to the increasing refinement of the turbulence structure with an increase in Reynolds number. The Taylor microscale increased significantly during acceleration, which may be attributed to the corresponding tendency of the turbulence fine structure to decay when subjected to strong acceleration. A similar increase was, however, also observed during deceleration. This appeared to be systematic, although it could be in part an artifact of cycle-to-cycle variations. A comparison of Taylor microscale values during acceleration and deceleration with corresponding values in steady flows, shown in Figure 4.24, also shows that, on average, transient values were somewhat larger than steady ones.

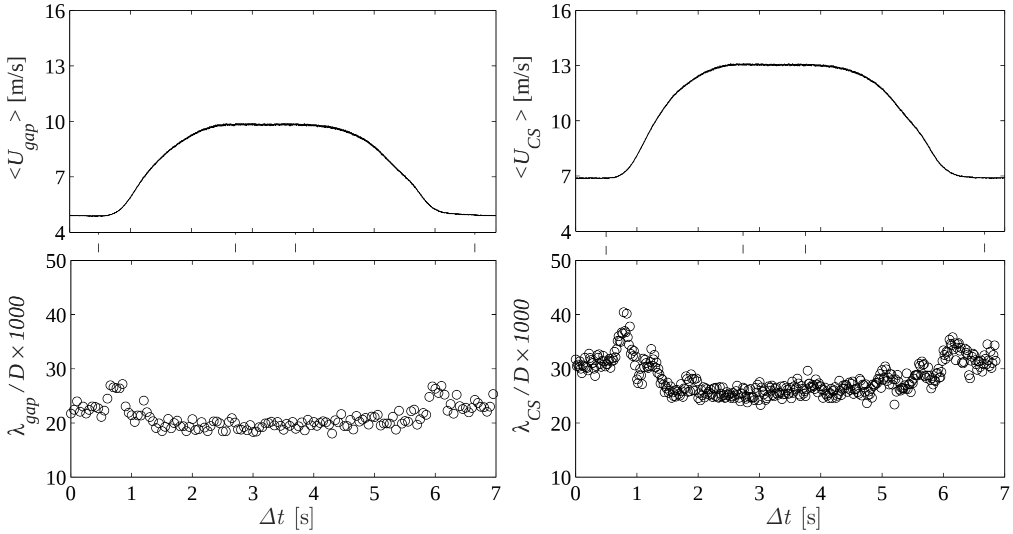

Figure 4.23: Variation of the axial Taylor microscale during the cycle at mid-gap (left) and in the central subchannel (right).

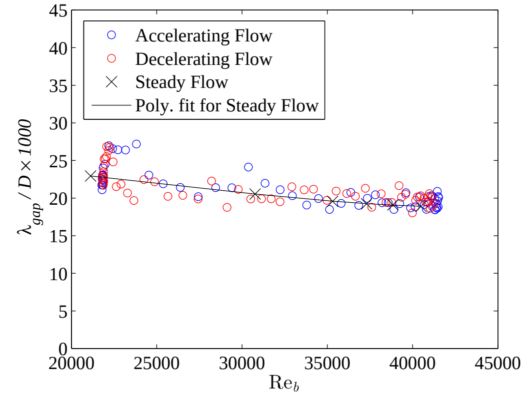

Figure 4.24: Axial Taylor microscale at different bulk Reynolds numbers at mid-gap (left) and in the central subchannel (right).

The turbulence Reynolds number is shown in Figures 4.25 and 4.26. On the average, deceleration increases the turbulence Reynolds number. Acceleration has a much weaker effect and seems to reduce on the average the turbulence Reynolds number.

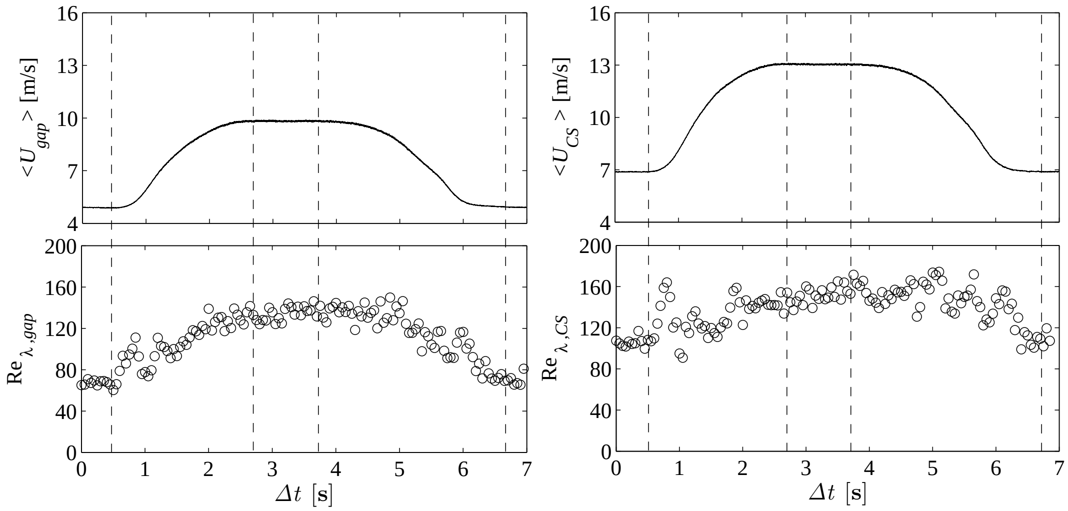

Figure 4.25: Turbulence Reynolds number during the cycle at mid-gap (left) and in the central subchannel (right).

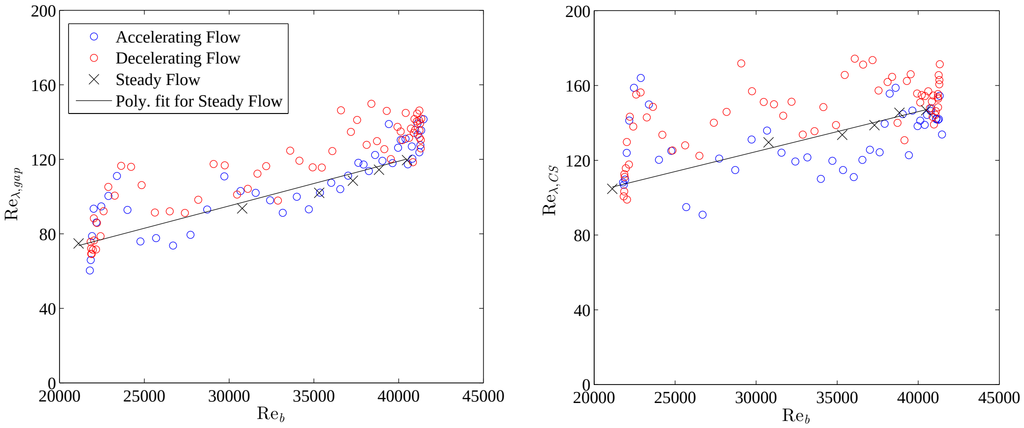

Figure 4.26: Turbulence Reynolds number at different bulk Reynolds numbers at mid-gap (left) and in the central subchannel (right).

4.2.6 Dissipation Rate and Kolmogorov Microscale

The estimated dissipation rate at mid-gap and in the central subchannel is shown in Figure 4.27. As turbulence was stronger at mid-gap than in the central subchannel, the dissipation rate was also stronger at mid-gap. Figure 4.28 shows that, at both locations, the dissipation rate during accelerating flow was significantly lower than that in equivalent steady flow, whereas the opposite was true for decelerating flow. Interestingly, during both acceleration and deceleration, the non-dimensional dissipation coefficient, shown in Figure 4.29, was much larger than that in steady flow.

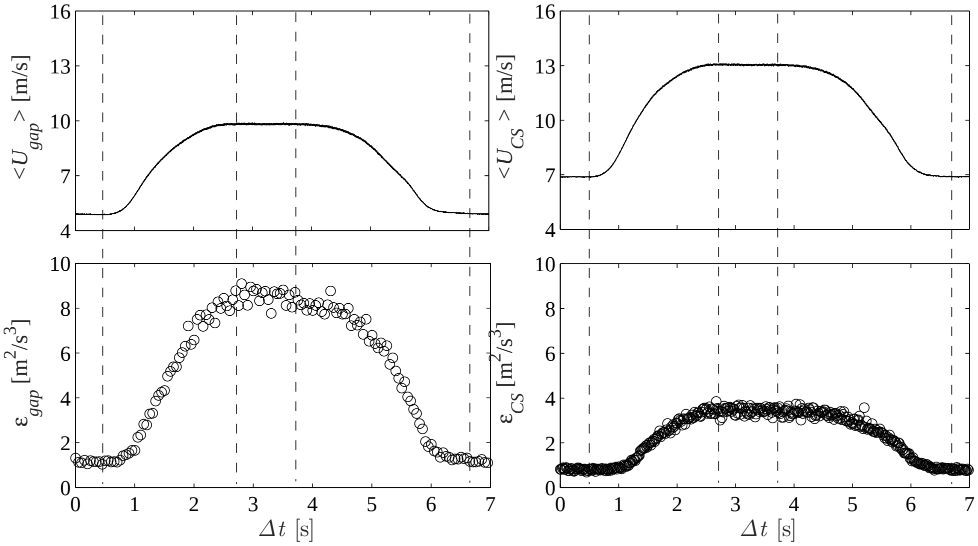

Figure 4.27: Turbulent dissipation rate during the cycle at mid-gap (left) and in the central subchannel (right).

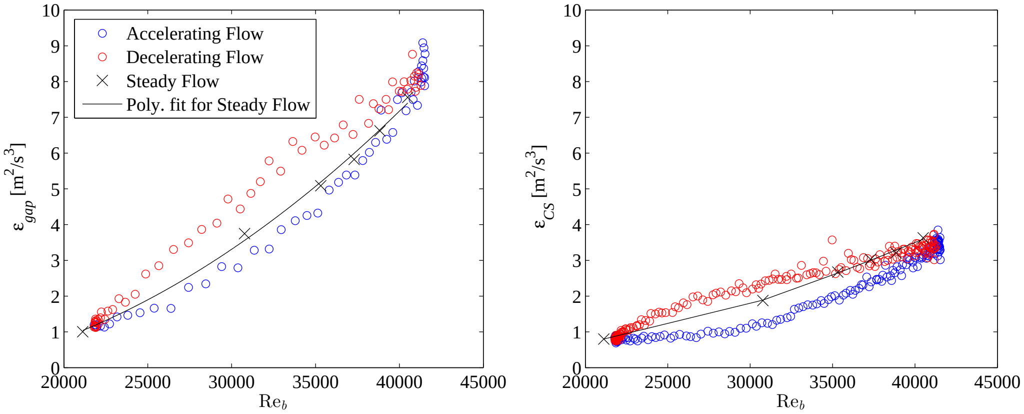

Figure 4.28: Turbulent dissipation rate at different bulk Reynolds numbers at mid-gap (left) and in the central subchannel (right).

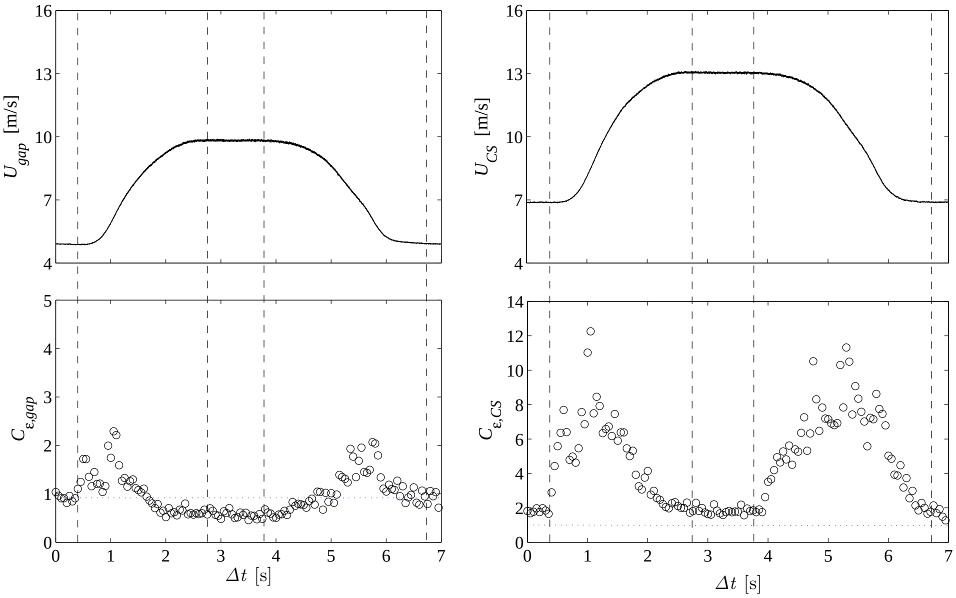

Figure 4.29: Dissipation coefficient during the cycle at mid-gap (left) and in the central subchannel (right).

The Kolmogorov microscale at mid-gap and in the central subchannel is shown in Figures 4.30 and 4.31. The values during accelerating flow were measurably higher than those in equivalent steady flow, whereas the opposite was true for decelerating flow. This means that acceleration tended to coarsen the turbulence fine structure, whereas deceleration tended to refine it, thus, extending the range of the energy cascade.

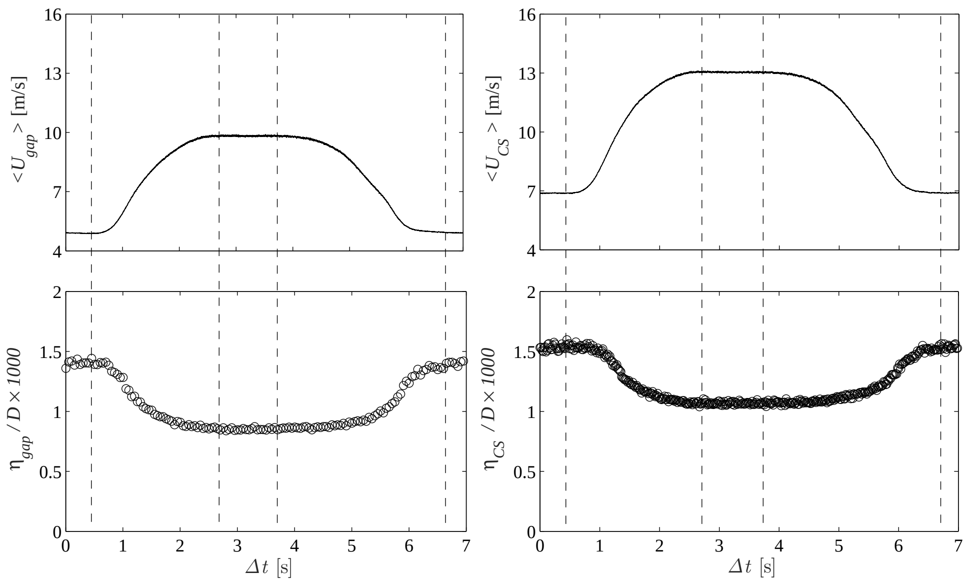

Figure 4.30: Kolmogorov microscale at different bulk Reynolds numbers at mid-gap (left) and in the central subchannel (right).

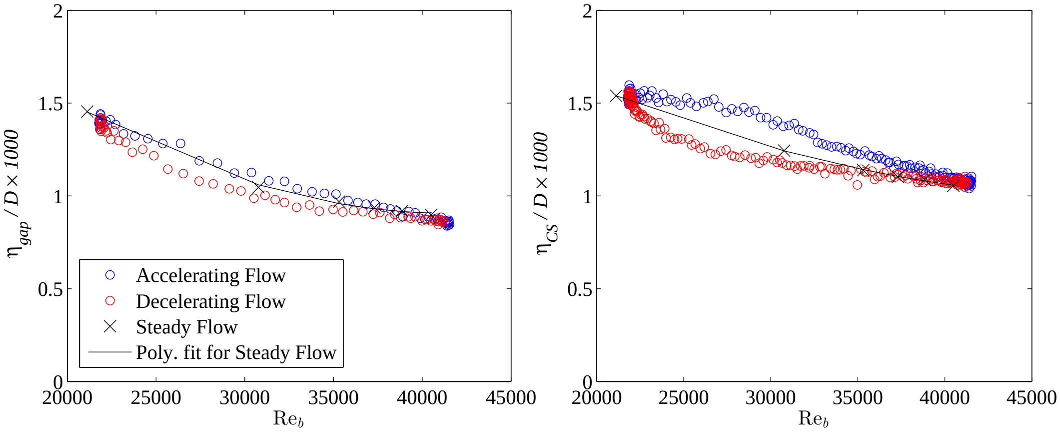

Figure 4.31: Kolmogorov microscale during the cycle at mid-gap (left) and in the central subchannel (right).

Chapter 5

Conclusions

5.1 Summary of Results

Some preliminary measurements were collected in stationary flows at a fixed bulk Reynolds number but with the bypass flap at two different positions. These results demonstrated that the position of the flap did not have a significant effect on the flow distribution and turbulence characteristics in the test section. These results were also in good agreement with measurements by Don (2016) in the same facility but before the installation of the bypass section.

The main set of measurements were collected while the flap was rotated periodically so that the flow in the test section consisted of four parts during each cycle: a stationary flow at a lower velocity, an accelerating flow, a stationary flow at a higher velocity, and a decelerating flow. Measurements of the instantaneous axial and azimuthal (with respect to the central rod) velocity components were collected at two locations: the middle of a rod-wall gap and the centre of the central subchannel. Data were recorded over 1500 cycles and phase-averaged in a manner that was synchronised with the position of the flap. A procedure to correct velocity fluctuations for cycle-to-cycle variations was devised and applied to the data.

The main conclusions of this work were as follows:

- The ratio of the phase-averaged mean velocities at the two locations was not affected significantly by cycle-to-cycle variations.
- By comparison to values in stationary flow at the same bulk Reynolds number, the gap vortex street Strouhal number was slightly larger during accelerating flow and smaller during decelerating flow.
- Cycle-to-cycle variation effects on the axial velocity fluctuations were particularly strong during deceleration, with the uncorrected velocity variances having unrealistically large values and the corresponding autocorrelation coefficient not reaching zero values within an extensive time interval.
- The integral length scale of the axial velocity at both locations during both acceleration and deceleration was larger than corresponding values in stationary flow.
- The Taylor microscale of the streamwise velocity during transients was slightly larger than corresponding stationary values.
- Compared to corresponding stationary values, the turbulent kinetic energy dissipation rate was larger for accelerating flow and smaller for decelerating flow. The opposite was true for the Kolmogorov microscale.

5.2 Recommendations for Future Work

A difficulty encountered in this study was the measurement of the bulk velocity during transients. Measurements of the unsteady velocity distribution in both the bypass exit and the inlet contraction throat are required to determine the unsteady bulk velocity. A proposed improvement would be to map out the profile using two single hot-wires, one to act as a reference point, and the other to measure the unsteady velocities at different points to map out a profile. The results at each point would be phase averaged and mapped together with the reference point. Other measurements that could be taken with the present facility would be to repeat this current study with different values of acceleration, in other words, increase the timescale of the accelerating and decelerating flow such as in Kang and Chang (2009). This would help verify the relationship between the values for the turbulence measurements presented in this study and the rate of acceleration or deceleration of the flow.

References

Bailey, S., 2006. The Interaction of a Wing-Tip Vortex and Free-Stream Turbulence. PhD Dissertation, University of Ottawa, Ontario, Canada.

Baratto, F., Bailey, S., Tavoularis, S., 2006. Measurements of frequencies and spatial correlations of coherent structures in rod bundle flows. Nucl. Eng. Des., 236, 1830–1837.

Blondeaux, P., Colombini, M., 1985. Pulsatile turbulent pipe flow. Proc. Fifth Symposium on Turbulent Shear Flows, Ithaca, NY. 15–21.

Brereton, G., Mankbadi, R., 1995. Review of recent advances in the study of unsteady turbulent internal flows. Appl. Mech. Rev., 48, 189–212.

Bruun, H., 1995. Hot-Wire Anemometry: Principles and Signal Analysis. Oxford; UK: Oxford University Press. ISBN 0198563426.

Chang, D., Tavoularis, S., 2005. Unsteady numerical simulations of turbulence and coherent structures in axial flow near a narrow gap. J. Fluid Mech., 127, 458–466.

Chang, D., Tavoularis, S., 2007. Numerical simulation of turbulent flow in a 37-rod bundle. Nucl. Eng. Des., 237, 575–590.

Chang, D., Tavoularis, S., 2012. Numerical simulations of developing flow and vortex street in a rectangular channel with a cylindrical core. Nucl. Eng. Des., 243, 176–199.

Chen, Y., Yang, C., Mao, Y., 2005. An experimental study of subcooled flow boiling critical heat flux of water under steady-state and flow-transient conditions at lower pressure. Proc. Eleventh International Topical Meeting on Nuclear Reactor Thermal-Hydraulics, Avignon, France.

Chun, S.-Y., Shin, C.-H., Hong, S.-D., Song, C.-H., 2009. Heat transfer characteristics near the critical pressure in a rod bundle cooled by R-134a fluid during pressure transient. Proc. Fourth International Symposium on Supercritical Water-Cooled Reactors, Heidelberg, Germany.

Cook, W., Murphy, J., Owen, F., 1985. An experimental and computational study of turbulent boundary layers in oscillating flows. Proc. Fifth Symposium on Turbulent Shear Flows. 13–18.

Cousteix, J., Houdeville, R., Javelle, J., 1981. Response of a turbulent boundary layer to a pulsation of the external flow with and without adverse pressure gradient. In R. Michel, J. Cousteix, R. Houdeville (Eds.), *Unsteady Turbulent Shear Flows,* 120–144. Toulouse, France: Springer.

Don, A., 2016. Structure of Turbulent Flow in a Rod Bundle. M. A. Sc., University of Ottawa, Ontario, Canada.

Eifler, W., Nijsing, R., 1967. Experimental investigation of velocity distribution and flow resistance in a triangular array of parallel rods. Nucl. Eng. Des., 5, 22–42.

El Tahry, R. S., 1990. Discussion of the role of coherent structures. In J. L. Lumley (Ed.), *Whither Turbulence? Turbulence at the Crossroads,* 170–191. Ithaca, NY: Springer.

Gerrard, J., 1971. An experimental investigation of pulsating turbulent water flow in a tube. J. Fluid Mech., 46, 43–64.

Greenblatt, D., Moss, E. A., 2004. Rapid temporal acceleration of a turbulent pipe flow. J. Fluid Mech., 514, 65–75.

Guellouz, M., Tavoularis, S., 2000. The structure of turbulent flow in a rectangular channel containing a cylindrical rod–part 1: Reynolds-averaged measurements. Exp. Therm. Fluid Sci., 23, 59–73.

He, K., Seddighi, M., He, S., 2016. DNS study of a pipe flow following a step increase in flow rate. Int. J. Heat Fluid Flow, 57, 130–141.

He, S., Jackson, J., 2000. A study of turbulence under conditions of transient flow in a pipe. J. Fluid Mech., 408, 1–38.

He, S., Jackson, J., 2009. An experimental study of pulsating turbulent flow in a pipe. Eur. J. Mech. B-Fluid, 28, 309–320.

He, S., Seddighi, M., 2015. Transition of transient channel flow after a change in Reynolds number. J. Fluid Mech., 764, 395–427.

He, S., Seddighi, M., Gorji, S., Mathur, A., 2015. Transition of transient turbulent channel flow. Procedia Engineer., 126, 34–38.

Hong, S.-D., Chun, S.-Y., Kim, S.-Y., Baek, W.-P., 2004. Heat transfer characteristics of an internally-heated annulus cooled with R-134a near the critical pressure. Nucl. Eng. Technol., 36, 403–414.

Hong, S.-D., Chun, S.-Y., Yoon, Y., Baek, W., 2003. Heat transfer characteristics of R-134a fluid during the pressure transient from supercritical pressure to subcritical pressure. Proc. Tenth International Topical Meeting on Nuclear Reactor Thermal Hydraulics, Seoul, Korea.

Hooper, J., Rehme, K., 1984. Large-scale structural effects in developed turbulent flow through closely-spaced rod arrays. J. Fluid Mech., 145, 305–337.

Hussain, A. F., 1983. Coherent structures - reality and myth. Phys. Fluids, 26, 2816–2850.

Jerome, F., Guitton, D., Patel, R., 1971. Experimental study of the thermal wake interference between closely spaced wires of a X-type hot-wire probe. The Aeronautical Quarterly, 22, 119–126.

Kang, K.-H., Chang, S.-H., 2009. Experimental study on the heat transfer characteristics during the pressure transients under supercritical pressures. Int. J. Heat Mass Transfer, 52, 4946–4955.

Kirmse, R., 1979. Investigations of pulsating turbulent pipe flow. J. Fluid Mech., 101, 436–442.

Lesieur, M., 1997. Turbulence in Fluids. In: Fluid Mechanics and its Applications, vol. 40, Springer, Dordrecht, Netherlands.

Maruyama, T., Kuribayashi, T., Mizushina, T., 1976. The structure of the turbulence in transient pipe flows. J. Chem. Eng. Jpn., 9, 431–439.

Meyer, L., 2010. From discovery to recognition of periodic large scale vortices in rod bundles as source of natural mixing between subchannels - a review. Nucl. Eng. Des., 240, 1575–1588.

Murphy, J., Prenter, P., 1981. A Hybrid Computing Scheme for Unsteady Turbulent Boundary Layers. Proc. Third Symposium on Turbulence Shear Flows, Davis, CA, USA. 9–11.

Nedić, J., Tavoularis, S., Marusic, I., 2017. Dissipation scaling in constant-pressure turbulent boundary layers. Phys. Rev. Fluids, 2, 032601–1–032601–7.

Ohmi, M., Kyomen, S., Usui, T., 1978. Analysis of velocity distribution in pulsating turbulent pipe flow with time-dependent friction velocity. Bull. of JSME, 21, 1137–1143.

Ohmi, M., Usui, T., 1976. Pressure and velocity distributions in pulsating turbulent pipe flow part 1 theoretical treatments. Bull. of JSME, 19, 307–313.

Pope, S. B., 2001. Turbulent Flows. Cambridge; UK: Cambridge University Press. ISBN 0521598869.

Ramaprian, B., Tu, S., 1980. An experimental study of oscillatory pipe flow at transitional Reynolds numbers. J. Fluid Mech., 100, 513–544.

Ramaprian, B., Tu, S., 1983. Fully developed periodic turbulent pipe flow. part 2. the detailed structure of the flow. J. Fluid Mech., 137, 59–81.

Rind, E., Tavoularis, S., 2012. Design, Instrumentation and Performance of a Large-scale Rod-Bundle Air Flow Facility. Technical Report UO-MCG- BF-2012- 01, University of Ottawa, Ontario, Canada.

Seddighi, M., He, S., Pokrajac, D., O'Donoghue, T., Vardy, A., 2015. Turbulence in a transient channel flow with a wall of pyramid roughness. J. Fluid Mech., 781, 226–260.

Seddighi, M., He, S., Vardy, A., Orlandi, P., 2014. Direct numerical simulation of an accelerating channel flow. Flow Turbul. Combust, 92, 473–502.

Shemer, L., Kit, E., 1984. An experimental investigation of the quasisteady turbulent pulsating flow in a pipe. Phys. Fluids, 27, 72–76.

Shemer, L., Wygnanski, I., Kit, E., 1985. Pulsating flow in a pipe. J. Fluid Mech., 153, 313–337.

Tardu, S. F., Da Costa, P., 2005. Experiments and modeling of an unsteady turbulent channel flow. AIAA J., 43, 140–148.

Tavoularis, S., 2005. Measurement in Fluid Mechanics. Cambridge; UK: Cambridge University Press. ISBN 9780521138390.

Tavoularis, S., 2011. Rod bundle vortex networks, gap vortex streets, and gap instability: A nomenclature and some comments on available methodologies. Nucl. Eng. Des., 241, 2624–2626.

Tu, S., Ramaprian, B., 1983. Fully developed periodic turbulent pipe flow. part 1. main experimental results and comparison with predictions. J. Fluid Mech., 137, 31–58.

Watanabe, N., Chun, S.-Y., Aritomi, M., Kikura, H., 2011. Experimental study on heat transfer characteristics of vertical 5x5 heated rod bundles around critical pressure with R-134a. J. Nucl. Sci. Technol., 48, 135–144.

Zhang, G., Al-Hawshabi, N. H. A., Yang, Y., 2011. Experimental study on the depressurization of freon at supercritical pressure. Proc. Fifth Int. Sym. SCWR, Vancouver, Canada.